

**PARTICLE IMAGE VELOCIMETRY IN A HIGH-PRESSURE TURBINE  
STAGE AT AERODYNAMICALLY ENGINE REPRESENTATIVE  
CONDITIONS**

by

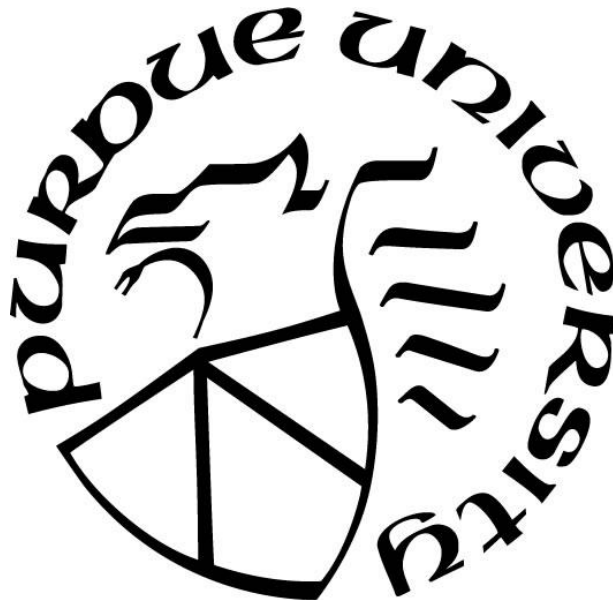
**Daniel C. Inman**

**A Thesis**

*Submitted to the Faculty of Purdue University*

*In Partial Fulfillment of the Requirements for the degree of*

**Master of Science in Aeronautics and Astronautics**



School of Aeronautics and Astronautics

West Lafayette, Indiana

May 2020

**THE PURDUE UNIVERSITY GRADUATE SCHOOL  
STATEMENT OF COMMITTEE APPROVAL**

**Dr. Guillermo Paniagua, Chair**  
School of Mechanical Engineering

**Dr. Terrence Meyer**  
School of Mechanical Engineering

**Dr. Nicole Key**  
School of Mechanical Engineering

**Approved by:**  
Dr. Gregory Blaisdell

*Dedicated to my wife, Hannah, for all the time and support she gave me regardless of her  
impossibly busy schedule in medical school; and to our families, who selflessly put both of our  
needs above their own.*

## ACKNOWLEDGMENTS

The author would like to acknowledge Dr. Guillermo Paniagua and the entire PETAL team for their dedication and guidance throughout this work. The author would also like to acknowledge the Rolls-Royce Corporation for their technical and financial support.

***Disclaimer:** The views expressed in this thesis are those of the author and do not reflect the official policy or position of the United States Air Force, Department of Defense, or the U.S. Government.*

# TABLE OF CONTENTS

LIST OF TABLES .....	6
LIST OF FIGURES .....	7
LIST OF ABBREVIATIONS.....	9
LIST OF SYMBOLS .....	10
ABSTRACT.....	11
1. INTRODUCTION .....	12
1.1 Review of Particle Image Velocimetry.....	13
1.2 Review of Previous Experimentation .....	14
1.3 Research Methodology .....	18
2. DEVELOPMENT OF MEASUREMENT TECHNIQUE .....	20
2.1 Facility Review .....	20
2.2 Design of Laser Delivery Probe.....	26
2.3 Experimental Methodology .....	28
2.4 Development of Data Processing Tool .....	33
3. EVALUATION OF METHODOLOGY IN ANNULAR CASCADE.....	38
3.1 First Application of Technique .....	38
3.2 Time-Averaged Flowfield Analysis.....	41
3.3 Assessment of High-Frequency Capabilities .....	46
3.4 Uncertainty Analysis.....	49
4. DEVELOPMENT OF OPTICAL SETUP FOR TIP FLOW MEASUREMENTS.....	52
4.1 Development of Endoscopic PIV in Annular Environment .....	54
4.2 Evolution of Setup for 3D Velocity Measurements.....	56
5. CONCLUSIONS .....	58
REFERENCES .....	60

**LIST OF TABLES**

Table 2.1. Flow parameters for the different measurement conditions. Tt: total temperature; Re: Reynolds number. .... 28

## LIST OF FIGURES

Figure 1.1. Standard setup for planar 2D PIV in a linear wind tunnel (reprinted by permission from Springer Nature) [1].	14
Figure 1.2. Experimental setup for SPIV at the transonic test turbine facility at Graz University of Technology (reprinted by permission from Springer Nature) [9].	16
Figure 1.3. Ensemble-averaged velocity recorded by SPIV for six stator-rotor positions at 10 600 rpm. A and B indicate two stator blades (reprinted by permission from Springer Nature) [9].	17
Figure 1.4. Schematic view of the PIV setups [12].	18
Figure 2.1. PETAL facility schematic.	21
Figure 2.2. Layout of the test article.	22
Figure 2.3. Locations for injecting seed particles into BRASTA. Left: Global and Semi-Global seeding locations. Right: Local seeding locations.	23
Figure 2.4. Images of illuminated seed particles with local seeding at cold test conditions from locations A (left) and B (right) of Figure 2.3.	24
Figure 2.5. Image of illuminated seed particles with semi-global seeding.	25
Figure 2.6. Sketch of the method used to deliver the laser sheet into the annular cascade targeting a field of view located at midspan in the passage. The location of the probe avoided perturbations to the flow at the measurement location.	26
Figure 2.7. Details of the laser delivery probe.	27
Figure 2.8. Flow path inside the test section and location of the test article.	29
Figure 2.9. PIV setup with camera and laser arrangement in the annular wind tunnel.	30
Figure 2.10. Frame straddling scheme.	31
Figure 2.11. CFD computational domain and interrogation areas for PIV-CFD comparison.	32
Figure 2.12. Details of the 5-hole probes used in BRASTA.	33
Figure 2.13. Image intensity as a function of the frame number.	34
Figure 2.14. Image pre-processing flowchart.	35
Figure 2.15. Number of centroids detected in image pair (31 <sup>st</sup> and 32 <sup>nd</sup> frames) as a function of contrast limit from vane2 experiment at hot test conditions.	36
Figure 2.16. Number of centroids detected in image pair (71 <sup>st</sup> and 72 <sup>nd</sup> frames) as a function of contrast limit from vane2 experiment at hot test conditions.	37
Figure 3.1. Alternate PCV lens location with respect to laser delivery probe.	38

Figure 3.2. Comparison of vector fields (A) before and (B) after implementing custom image pre-processing techniques on the vane 1 experiment at cold conditions. ....	39
Figure 3.3. Time-averaged velocity contour in a preliminary evaluation of the flow of the vane1 experiment at cold test conditions with streamlines. ....	40
Figure 3.4. Correlation map for a velocity vector from vane1 configuration at cold test conditions. ....	41
Figure 3.5. Time-averaged velocity contour of the flow of the vane2 experiment at cold test conditions with streamlines from (A) experimental measurements and (B) CFD model predictions. ....	42
Figure 3.6. Time-averaged flow angle contour of the flow of the vane2 experiment at cold test conditions from (A) experimental measurements and (B) CFD model predictions. ....	43
Figure 3.7. Time-averaged velocity contour of the flow of the vane2 experiment at hot test conditions with streamlines from (A) experimental measurements and (B) CFD model predictions. ....	44
Figure 3.8. Time-averaged flow angle contour of the flow of the vane2 experiment at hot test conditions from (A) experimental measurements and (B) CFD model predictions. ....	45
Figure 3.9. Comparison of the flow exit angle at the middle of the passage measured with a 5-hole probe and the CFD prediction. ....	46
Figure 3.10. Flow angle time series of vane2 configuration at cold test conditions. ....	47
Figure 3.11. The number of vectors calculated across a single image set of the vane2 configuration at (A) cold and (B) hot test conditions. ....	48
Figure 3.12. Percent uncertainty from correlation bias error for a vector time series of the vane2 configuration at cold conditions. ....	50
Figure 3.13. Sample standard deviation from vector time series of vane2 configuration at cold conditions. ....	51
Figure 4.1. Configuration of STARR turbine module. ....	52
Figure 4.2. Sketch of the proposed method to deliver the laser sheet into STARR and image the rotor passage with two borescopes to perform SPIV. ....	53
Figure 4.3. Laser and camera configuration for endoscopic PIV in BRASTA. ....	54
Figure 4.4. Details of the BRASTA borescope mount. ....	55
Figure 4.5. Details of the STARR borescope mount. ....	56
Figure 4.6. Details of the STARR laser delivery inserts. ....	57

## LIST OF ABBREVIATIONS

BRASTA:	Big Rig for Annular Stationary Turbine Analysis
CFD:	Computational Fluid Dynamics
FOV:	Field of View
HSV:	Horseshoe Vortex
Nd:YAG:	Neodymium-doped Yttrium Aluminum Garnet
PCV:	Plano-Concave
PCX:	Plano-Convex
PETAL:	Purdue Experimental Turbine Aerothermal Laboratory
PIV:	Particle Image Velocimetry
PS:	Pressure Side
RANS:	Reynolds-averaged Navier Stokes
SPIV:	Stereoscopic Particle Image Velocimetry
SS:	Suction Side
SST:	Shear Stress Transport
STARR:	Small Turbine Aerothermal Rotating Rig
TRL:	Technology Readiness Level
vane1:	First-stage High Pressure Turbine Stator Profile
vane2:	First-stage High Pressure Turbine Stator Profile

## LIST OF SYMBOLS

$C_x$ :	Axial chord
$Re$ :	Reynolds number
$T$ :	Temperature
$V$ :	Velocity
$\dot{m}$ :	Mass flow rate
$k$ :	Turbulence kinetic energy
$s$ :	Sample standard deviation
$t$ :	Time
$\Delta$ :	Change
$\omega$ :	Turbulence specific dissipation rate
$\varepsilon$ :	Turbulent kinetic energy dissipation rate

### Subscripts

$max$ :	Maximum
$t$ :	Total

## ABSTRACT

Particle Image Velocimetry (PIV) is a well-established technique for determining the flow direction and velocity magnitude of complex flows. This paper presents a methodology for executing this non-intrusive measurement technique to study a scaled-up turbine vane geometry within an annular cascade at engine-relevant conditions. Custom optical tools such as laser delivery probes and imaging inserts were manufactured to mitigate the difficult optical access of the test section and perform planar PIV. With the use of a burst-mode Nd:YAG laser and Photron FASTCAM camera, the frame straddling technique is implemented to enable short time intervals for the collection of image pairs and velocity fields at 10 kHz. Furthermore, custom image processing tools were developed to optimize the contrast and intensity balance of each image pair to maximize particle number and uniformity, while removing scattering and background noise. The pre-processing strategies significantly improve the vector yield under challenging alignment, seeding, and illumination conditions. With the optical and software tools developed, planar PIV was conducted in the passage of a high-pressure stator row, at mid-span, in an annular cascade. Different Reynolds number operating conditions were achieved by modifying the temperature and mass flow. With careful spatial calibration, the resultant velocity vector fields are compared with Reynolds Averaged Navier Stokes (RANS) simulations of the vane passage with the same geometry and flow conditions. Uncertainty analysis of the experimental results is also presented and discussed, along with prospects for further improvements. Lastly, the adaptations of the diagnostic technique needed to assess rotor tip technology in a rotating facility are detailed.

# 1. INTRODUCTION

With the advancement of turbomachinery design and optimization, improvements in the performance of turbines are measured in fractions of points of efficiency. The quantification of secondary and tip flow phenomena is central to understanding the principal loss mechanisms of each turbine stage. Horseshoe, passage and tip leakage vortices play a large role in the performance of turbine airfoils and their efficiency. If the behavior of these flow features is not well understood, it can lead to incorrect performance predictions and ultimately sub-optimal designs. As the aviation and power generation industries trend more toward small core turbines, these secondary flows become proportionally more important in determining efficiency and can occur at even higher frequencies. This inspired the first objective of this work, which is to develop the tools needed to assess a new vane geometry and turbine tip for small engine cores.

CFD is frequently used to predict the behavior of these environments, but until these solutions exceed the accuracy of empirical measurements, higher resolution and less invasive diagnostic techniques are required. Physical probes can be used to anchor CFD simulations to a degree, but their discrete nature leads to low spatial resolution, and their finite size means that they inherently disturb the flow they are made to measure. This is especially true in small core turbines, where rake sizes can be significant compared to the size of the airfoils themselves. To combat this problem, Particle image velocimetry (PIV) can be employed as a non-intrusive measurement technique with high-frequency capabilities to helpfully reveal the physical phenomena related to those secondary flow structures. While PIV is well developed in fundamental applications, barriers to implementation in turbine test facilities still exist. Consequently, the second objective of this paper is to advance current optical diagnostic techniques for use in resolving turbine flowfields with high spatial resolution and high-frequency capabilities in high TRL research facilities.

The objectives of this study are summarized below:

1. Develop tools to assess a new vane geometry and turbine tip, for small engine cores, which call for non-intrusive technologies and exhibit high frequency phenomena
2. Advance optical diagnostics to resolve turbine flowfield with high spatial and temporal resolution

## 1.1 Review of Particle Image Velocimetry

Since its original conception, PIV has been modified and adapted to study a wide variety of flowfields in turbomachinery. PIV generally consists of an arrangement where the laser illumination sheet is perpendicular to the camera location. For this reason, applications to linear cascades and traditional wind tunnels have been thoroughly explored. Conversely, its implementation in annular turbine cascades becomes more challenging due to the more limited optical access and the annular geometries. Furthermore, the high velocities encountered in high pressure turbines require high camera repetition rates. Additional difficulties are experienced with these cases including lower contrast particle images, and lower image resolution which can result in potentially unresolved velocity vector fields. This can necessitate time or ensemble averaging and limits flow analysis to steady or instantaneous phenomena; therefore, the capabilities of PIV in high pressure turbines have not been fully realized.

The basic process to perform PIV begins with the injection of tracer particles into the flow upstream of the region of interest. A laser sheet, like the one depicted in Figure 1.1, is used to illuminate the particles within that region of interest so that they can be captured in an image. With a very short pulse width, the image resolves an instantaneous array of the tracer particles. With a series of images taken, the frames are divided into subregions and the displacement of the particles within these regions between two consecutive images can be determined through a cross-correlation algorithm. The known time between the laser pulses is then used to convert the displacement into velocity.

The resolution of the velocity measurements is dictated by the size of subregions, which is a parameter known as the window size and is selected by the user. A displacement vector is produced for each window; hence, greater spatial resolution is achieved by minimizing the size of the window. Conversely, smaller windows can decrease the quality of the correlation signal as they become more sensitive to variations in image intensity. Aside from increasing the uncertainty of the particle displacement, the cross-correlation program can fail to resolve the displacement vector if the differences are too great. According to Raffel et al. [1], non-uniform illumination creates noise in the correlation plane and the correlation peaks are skewed by the brightest particles. Xue et al. [2] affirm that the strength of the signal-to-noise ratio governs the accuracy and uncertainty of the cross-correlation and the resulting velocity measurements. To normalize the particle intensity and improve the quality of the cross-correlation signal, several different image

pre-processing techniques such as background subtraction, image binarization, intensity capping, and filtering have been explored [1]. Due to the added challenges posed by operating PIV in an annular turbine test section, a tailored image enhancement tool was implemented in the processing of the images acquired for this investigation.

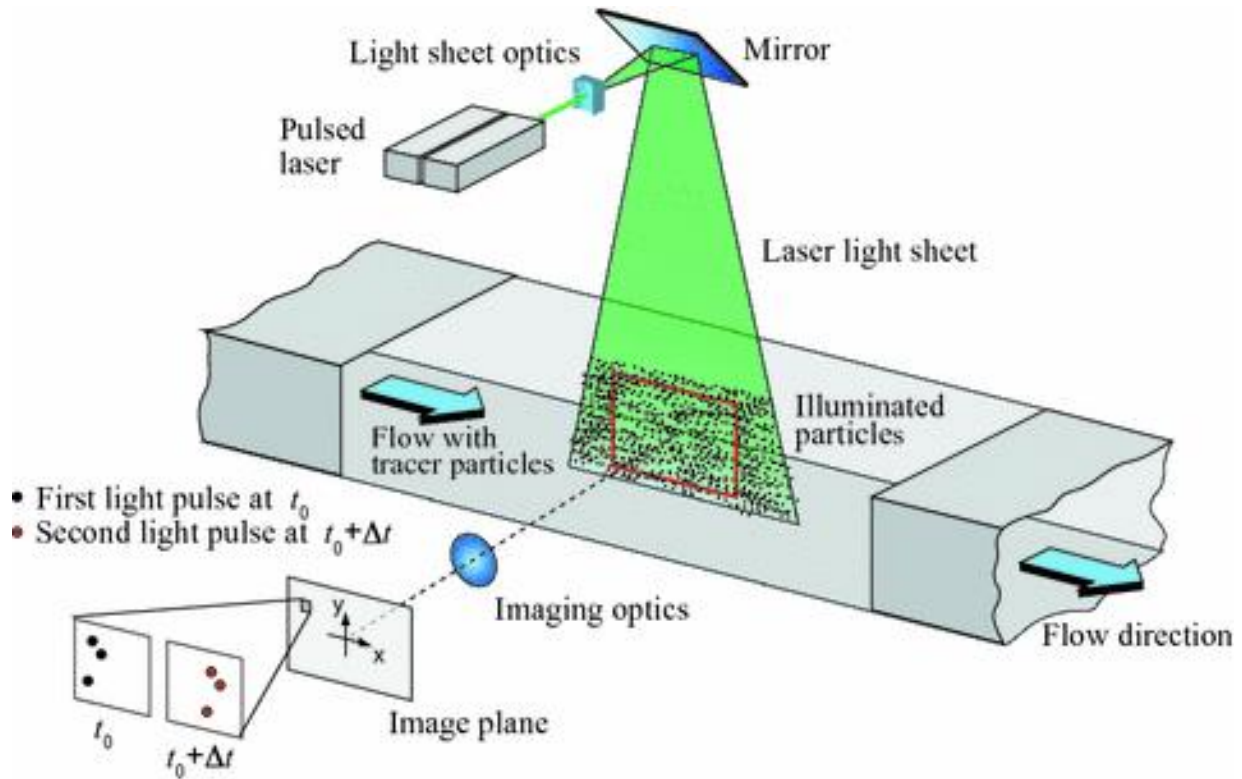


Figure 1.1. Standard setup for planar 2D PIV in a linear wind tunnel (reprinted by permission from Springer Nature) [1].

## 1.2 Review of Previous Experimentation

In lower Reynolds number experimentation, low repetition rates on the order of 10 Hz are used to investigate time-averaged flow structures with high-resolution cameras. Bloxham [3] conducted planar PIV on the leading edge of a cylinder in an open-loop linear wind tunnel to visualize the effects of endwall suction on the horseshoe vortex formation. This was achieved using a dual head Solo 120mJ Nd:YAG laser mounted to a three-axis traverse that delivers a laser sheet through clear acrylic tunnel walls. This setup affords the user a high degree of maneuverability in terms of the location and alignment of the laser sheet.

Several different authors have focused their efforts on characterizing the flow phenomena on turbomachinery representative geometries at these low Reynolds numbers with similar setups. Marks et al. [4] used a curved laser-sheet in the AFRL low-speed wind tunnel to match the curvature of the aft portion of the pressure side (PS) of the LPT blade to help characterize the transition region. The curved laser sheet was produced through the addition of a convex cylindrical lens oriented at an angle to the optical path after sheet forming optics. The angle and physical properties of the lens can be varied to match the curvature of any surface. This allows for axial velocity measurements in curved flow paths.

In this same low-speed wind tunnel, Gross et al. [5] and Bear et al. [6] used stereoscopic PIV (SPIV) to track the passage vortex and the suction side (SS) corner separation vortex on L2F turbine blades. SPIV is an adaptation of the traditional PIV setup where two cameras are used to record the same region of interest from two off-axis perspectives, which enables the calculation of all three spatial components of the velocity vectors within the image plane during post-processing. Velocity measurements axial to the flow direction were obtained at multiple locations within the passage and aft of the passage through the use of a low-repetition-rate double pulse laser and two PCO 1600 cameras fitted with Scheimpflug adapters to correct for the camera lens plane not being parallel to the image plane. [6] reports a laser sheet thickness of 1.5 mm to limit the average in-plane particle movement between exposures to less than 30% of the sheet thickness.

For higher Reynolds number applications in annular cascades and rotating rigs, PIV is performed at frequencies of 1 kHz or faster to try to resolve unsteady phenomenon. Peter et al. [7] performed time-averaged and time-resolved SPIV at 5 kHz on a compressor annular cascade to investigate rotating instability at a chord based Reynolds number of  $3 \times 10^5$ . Two Photron FASTCAMS SA1.1 operating at 10 kfps on tilt mounts were used to capture multiple 3D velocity fields tangential to the stator hub, which was coated with rhodamine b-doped paint to minimize light scattering. Time-resolved pressure data was collected in parallel with the SPIV measurements to serve as a reference for the correlation algorithm and to support the spectral analysis of the optical results. Time-resolved SPIV was also implemented by Anderson et al. [8] to characterize the unsteadiness of the HSV system in a low aspect ratio pin-fin array at a Reynolds number of  $2.0 \times 10^4$ . Two high speed cameras and a dual-head laser were used to produce vector fields at a sampling frequency of 1 kHz.

A comprehensive review of recent PIV measurements in rotating turbomachinery applications was performed by Woisetschläger and Göttlich [9], with a special focus on the facilities at Graz University of Technology and at German Aerospace Center DLR. The transonic test turbine facility at Graz University features 24 stator and 36 rotor blades rotating at 10,600 rpm, while the centrifugal compressor at German Aerospace DLR features 13 main and 13 splitter blades rotating at up to 50,000 rpm. Both facilities utilize a periscope-type laser delivery probe to deliver a laser sheet into the laser complex geometric environment, as well as a large optical window to allow two cameras to image the plane of interest so that SPIV can be performed. This configuration is illustrated in Figure 1.2.

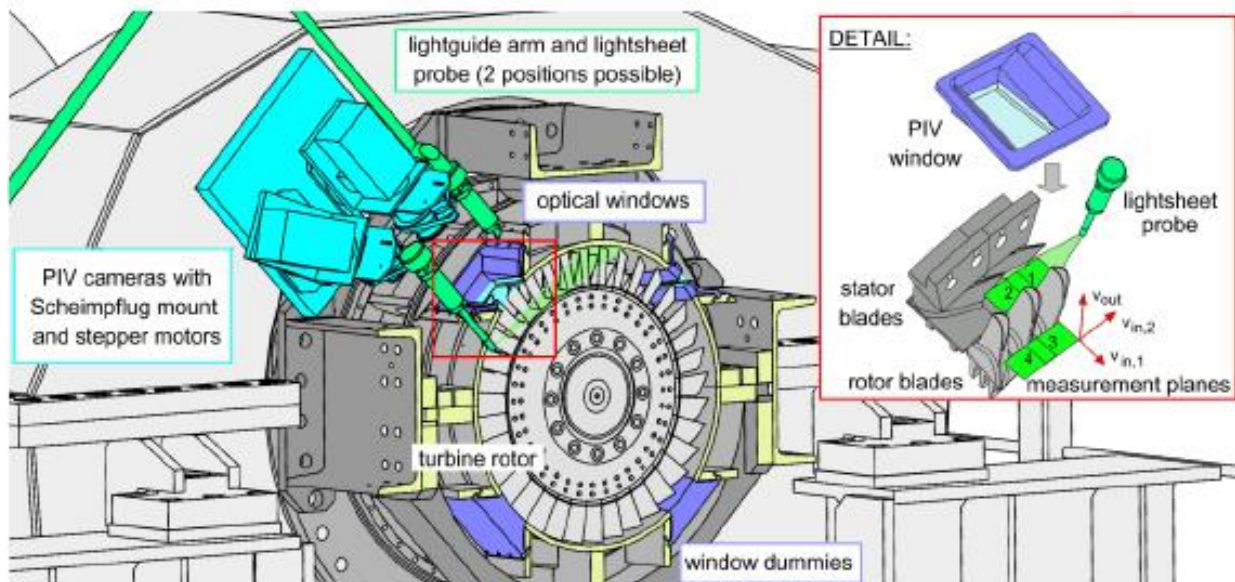


Figure 1.2. Experimental setup for SPIV at the transonic test turbine facility at Graz University of Technology (reprinted by permission from Springer Nature) [9].

Compressed air is used to purge the laser probe so that the internal optics are cooled and protected from the seeding oil. The results were ensemble-averaged to improve the resolution of velocity vectors within the imaged planes as shown in Figure 1.3. With this technique, the profiles of the wakes for both the stator and rotor rows are completely captured.

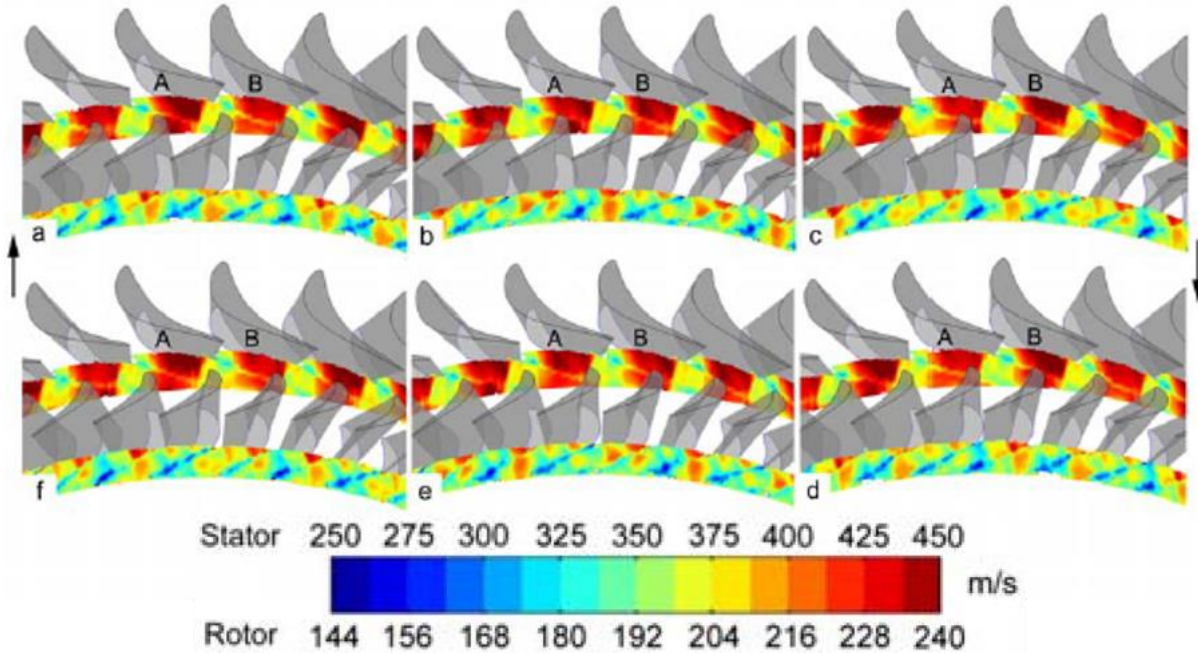


Figure 1.3. Ensemble-averaged velocity recorded by SPIV for six stator-rotor positions at 10 600 rpm. A and B indicate two stator blades (reprinted by permission from Springer Nature) [9].

Gostelow et al. [10] studied various secondary flow vortices in a transonic turbine cascade using temperature and pressure measurements from physical probes and sensors. The experiments were performed at an engine accurate Reynolds number of  $2.13 \times 10^5$ . The shedding frequency of the trailing edge vortex was estimated to be 10 kHz and given the Nyquist Theorem, PIV data would need to be acquired at a minimum of 20 kHz to characterize this unsteady flowfield; however, total temperature measurements were acquired at a rate of almost 100 kHz to resolve the energy separation. To study small core turbine designs, Cuadrado et al. [11] have developed a modular two-stage turbine rig that is capable of operating at rotational speeds of over 15,000 rpm. The Purdue Small Turbine Aerothermal Rotating Rig (STARR) will couple optical and intrusive measurements to precisely characterize stator and rotor flowfields at engine representative conditions. Based on previous experimentation, optical measurements will need to be acquired at frequencies in excess of 100 kHz to accurately characterize the unsteady phenomena present in small core turbines. One of the proposed optical measurement techniques presented in [11] is further detailed in this paper.

Due to the limited access of annular turbine rigs, endoscopic PIV was developed so that optical access can still be provided for the imaging equipment without the need for a large viewing

window. Kegalj and Schiffer [12] demonstrated the viability of acquiring PIV data in a 1.5 stage axial low-pressure turbine rig while imaging through a borescope. An axial (setup R) and tangential (setup C) plane were captured in the turbine annulus between the first rotor row and second stator row, illustrated in Figure 1.4, using the LaVision Imager ProX 2m camera and a 15 Hz dual cavity Nd:YAG laser. The results were time-averaged to overcome non-uniform illumination of the area of interest. A drawback to imaging through a borescope is that it bottlenecks the amount of light that reaches the camera chip, so the distance between the borescope and laser sheet must be minimized at the cost of the field of view. The signal to noise ratio was also improved by using larger seeding particles on the order of 2-3  $\mu\text{m}$ . Reeves and Lawson [13] present a method for evaluating and correcting the perspective errors associated with endoscopic PIV, with applications to stereoscopic arrangements.

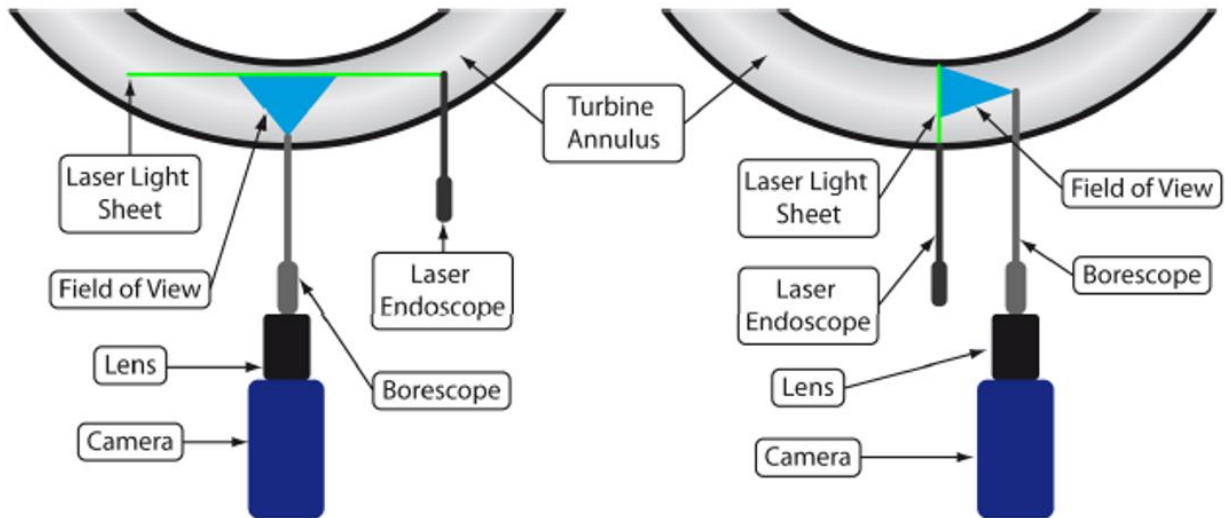


Figure 1.4. Schematic view of the PIV setups [12].

### 1.3 Research Methodology

To achieve the objectives, first the optical setup and data processing tools needed to perform non-intrusive measurements in an annular rig were developed. Conducting PIV in this environment required optical access to the region of interest, seeding in the desired portion of the annulus, precisely aligned optics, synchronized imaging, and a custom image pre-processing system to maximize the vector yield from the acquired images.

This optical setup is then applied to an annular scaled-up small core turbine vane passage at aerodynamically engine representative conditions. An initial validation of the experimental

design is performed on a set of turbine vanes referred to as vane1. After troubleshooting the procedures, the methodology is then applied to a second set of vanes, vane2, and compared to CFD model predictions of the velocity magnitude, flow angle, and their spatial distributions in the same geometry and flow conditions. Experimental probe measurements are also used to independently verify the accuracy of CFD model predictions of the flow angle at a separate location. The characteristics of the time-resolved results are also assessed, along with the prospects and challenges for high-speed flow measurements.

Lastly, tools were developed for facilitating the characterization of tip leakage flows in a rotating facility designed for evaluating new tip technologies. The setup evaluated in the annular cascade is advanced to enable 3D velocity measurements in the rotor passage and to acquire them endoscopically.

## **2. DEVELOPMENT OF MEASUREMENT TECHNIQUE**

The diagnostic complexities demanded a thorough approach to the instrumentation development, as well as the experimental design. This process began with a review of the optical access provided by the annular test section to select the velocity plane of interest. Based on the available access, a custom optical tool was developed to deliver the laser to desired location in the form of a thin sheet. Alignment procedures were then created to establish an accurate and consistent method of delivering the laser to the interrogation plane, in addition to ensuring the laser sheet and camera imaging plane are coplanar. Finally, an image post-processing tool was generated that enhances the quality of the PIV images to improve the detection of particles in the cross-correlation software.

### **2.1 Facility Review**

To assess the abatement of secondary flows, a stationary annular cascade (BRASTA) was developed at PETAL [14]. The facility is three times larger than the designed scale to facilitate higher spatial resolution measurements. The proposed optical diagnostic method was evaluated in the test section of BRASTA as this facility is being used to evaluate the performance of the new compact turbine vane geometries. A schematic of the entire PETAL facility is provided in Figure 2.1.

To operate the facility, dry air is stored at 150 bar in a 56 cubic meter air storage. The supply to the wind tunnel consists of two fluid lines coming from the air storage. The first line travels through a heater, allowing for control of mass flow and temperature. The second line is only controlled for mass flow and is unheated. A wide range of temperatures and mass flows can be achieved in the test section by independently varying the mass flows in each stream and the temperature at the exit of the heater. A mixing T-manifold is used to combine the streams before delivery to the facility. The warm non-vitiated dry air mass flow is then monitored through a calibrated critical flow Venturi.

During the start-up procedure, the desired flow conditions are stabilized while discharging the gradually warmer flow through an atmospheric purge line. Once the desired test conditions are

reached, the warm flow is diverted towards the wind tunnel using a fast-acting valve. The flow passes through a settling chamber for flow straightening and elimination of large turbulent structures coming from upstream piping components before entering the test section, where the test article is installed. Further downstream, the flow passes through a sonic throat used to independently set the Reynolds and Mach numbers inside the test section before exiting to a dump tank.

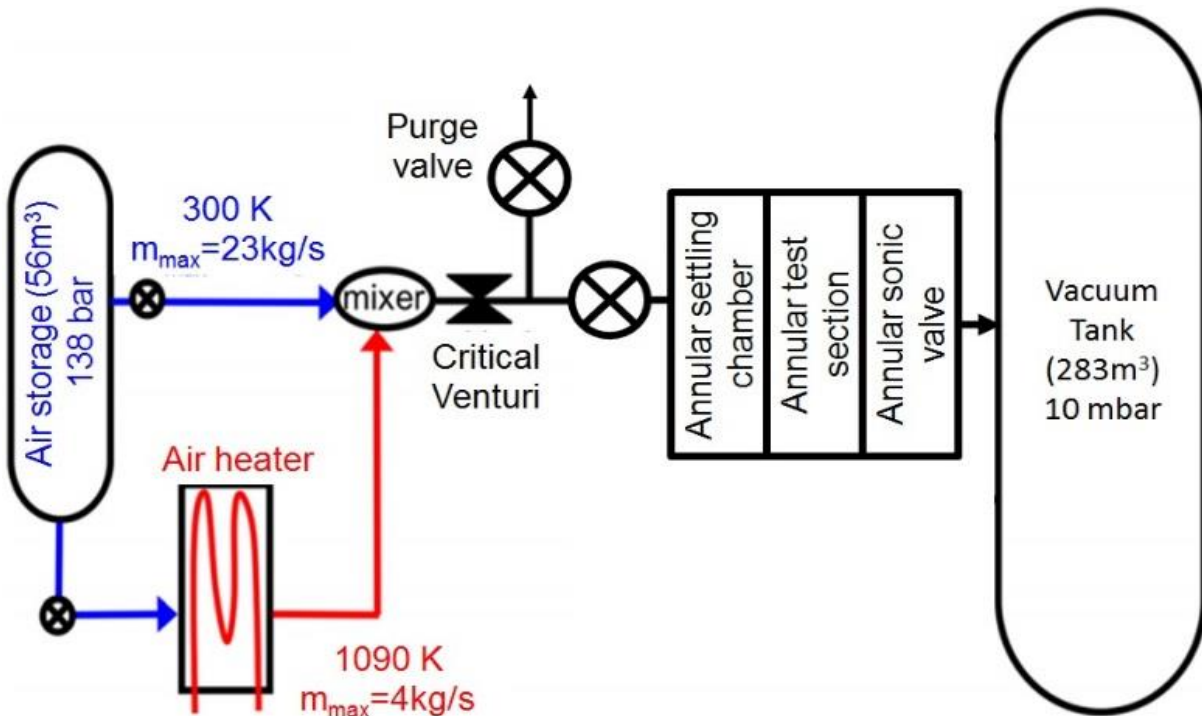


Figure 2.1. PETAL facility schematic.

Due to the added alignment complexities associated with conducting PIV in an annular cascade, not only were custom optical tools tailor-made for the testing rig, but the test section and test article were also designed to facilitate the execution of optical diagnostic techniques. This ensured suitable access for laser delivery and imaging at several locations along and across the test section. The test article for the present study is a scaled-up version of a first-stage high pressure turbine stator row. Figure 2.2 shows the annular cascade with the different features that were introduced into the design to perform PIV measurements. Detail A depicts the locations of the optical access, which are found in three different axial locations along the vane passage. To reduce light scattering within the passages with optical access, the surrounding aluminum surfaces were

coated with Cerakote matte black ceramic paint rated to 1200°F, as shown in detail B (Cerakote C-192P).

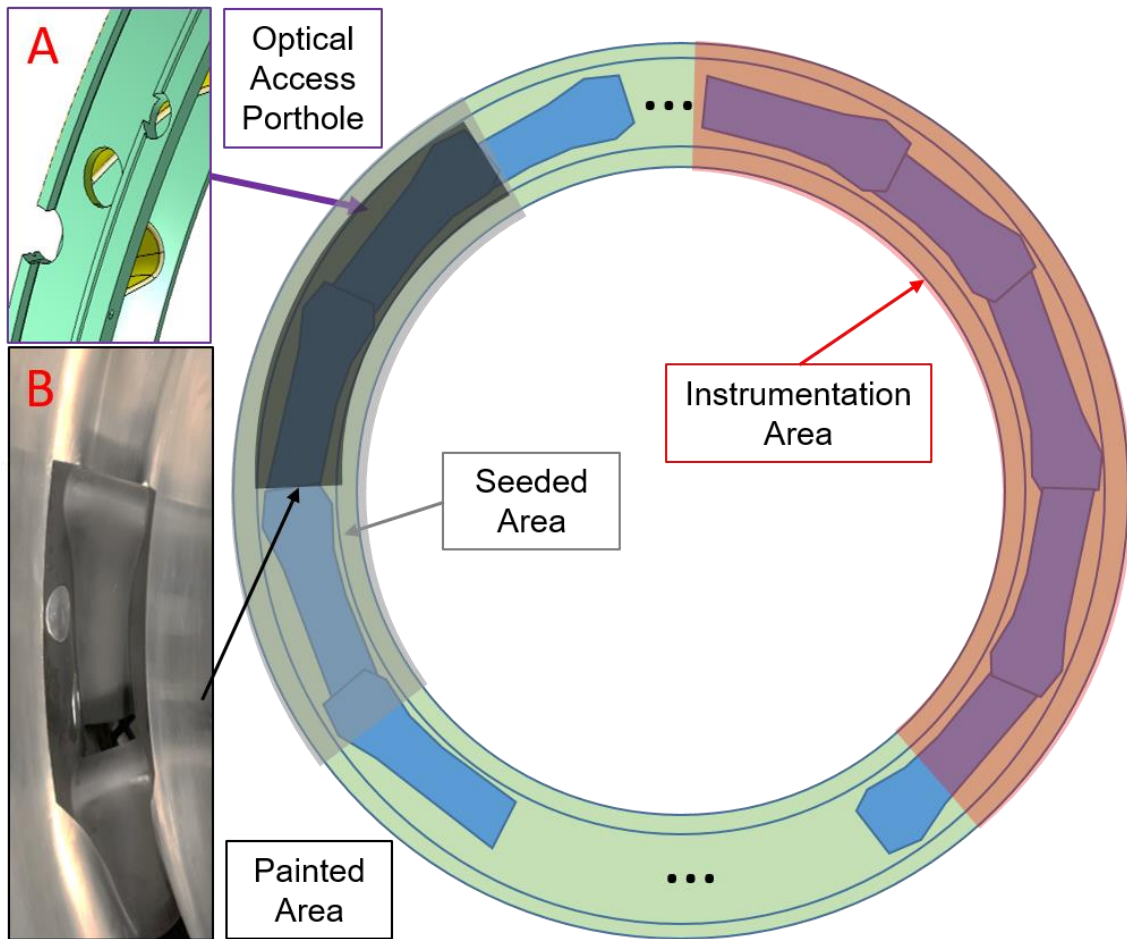


Figure 2.2. Layout of the test article.

Several strategies were examined for seeding particles into the flow. The modularity of the test section and the rig, in general, allows for local, semi-global, and global seeding of the test section flow path. Global seeding can be generated by locating the seeder just upstream of the fast-acting valve as indicated in Figure 2.3 (left). This would allow the seed particles to mix homogeneously with the entire air massflow in the settling chamber ; however, this global seeding incurs the risk of damaging the local instrumentation used to monitor flow conditions during the test (see Figure 2.2). For this reason, global seeding was not implemented in any test campaign. Semi-global seeding is produced by injecting particles through one of the ports on the upstream face of the settling chamber. This allows the seed particles to mix with the air exiting the left side

of the radial discharge manifold. Lastly, local seeding can be achieved by injecting particles into the holes at the test section inlet indicated in Figure 2.3 (right).

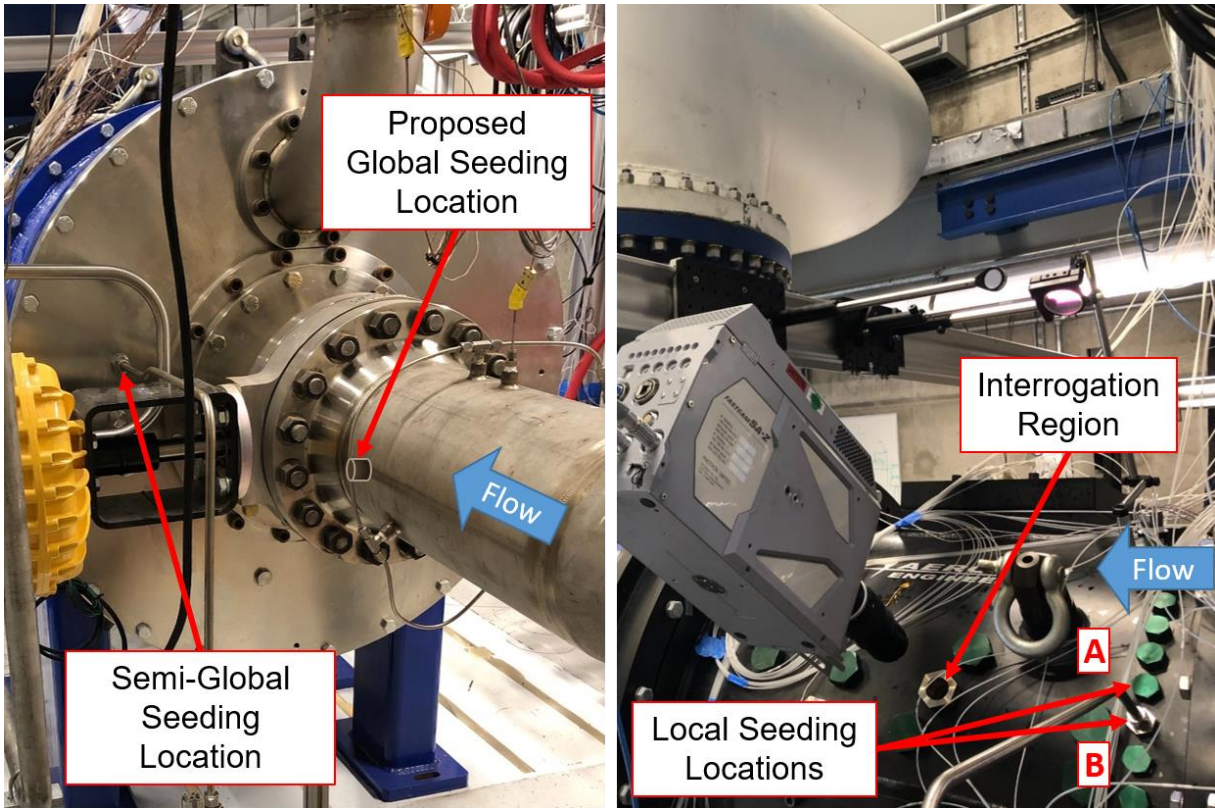


Figure 2.3. Locations for injecting seed particles into BRASTA. Left: Global and Semi-Global seeding locations. Right: Local seeding locations.

In attempt to minimize the contamination of the test section by the seeding oil, local seeding was the first location evaluated. Two separate ports, indicated by A and B in Figure 2.3, were assessed at 11.3 kg/s and 278 K. A sample frame from one of the image sets collected with seeding through port A is shown in Figure 2.4 (left). Not only is the seeding limited to the upper left portion of the window, it is also too dense to distinguish individual particles. Additionally, the seeding is not well mixed as revealed by the streamlike flow structures found within the atomized mineral oil. To ensure this outcome was not a consequence of the local seeding port selection, a second set of tests was conducted with the seed particles entering the test section through port B. As can be seen in Figure 2.4 (right), a similar result was attained: the seeding is not well mixed, it is limited to a median height of the window, and individual particles are hard to differentiate. Due to the proximity of the local seeding ports to the optical access window, the particles did not have

sufficient time to disperse into the whole stator passage and thus were concentrated too highly in smaller regions of the flow. These limitations in particle mixing impede the collection of high-quality data.

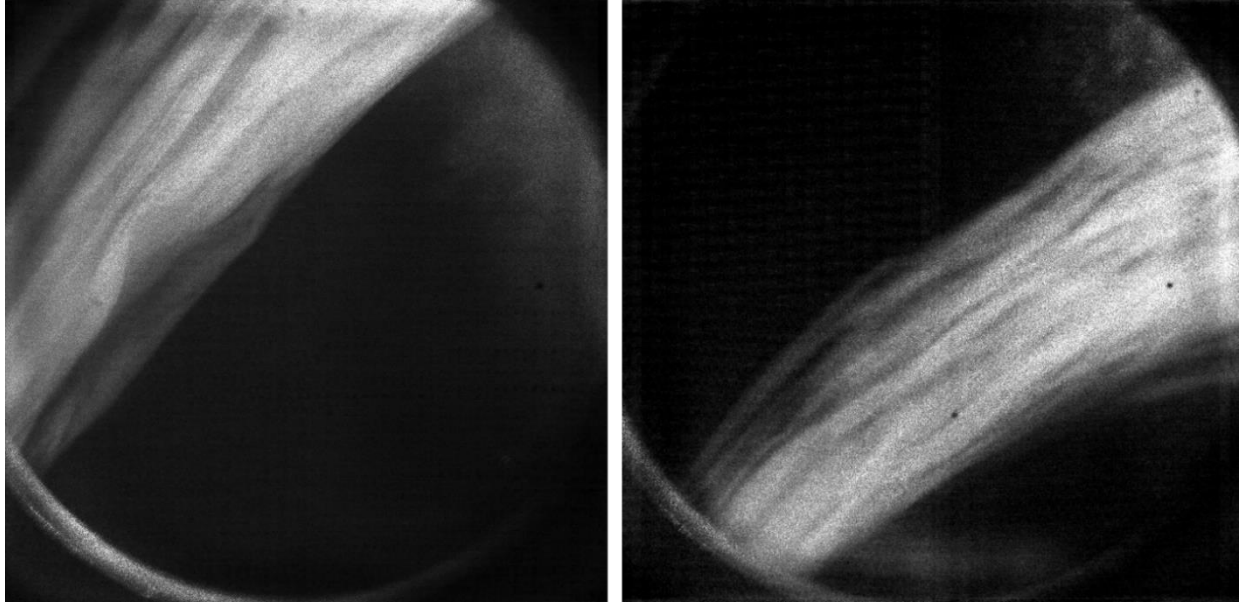


Figure 2.4. Images of illuminated seed particles with local seeding at cold test conditions from locations A (left) and B (right) of Figure 2.3.

Alternative local seeding approaches could have been pursued, such as injecting the seed particles into ports A and B simultaneously or manufacturing a dispersion nozzle, but the former does not resolve the mixing problem and the latter creates an obstruction in the flow just upstream of the stator passage. To minimize particle interference from injection and ensure proper seeding density, the seeder was interfaced into the wind tunnel in the settling chamber upstream of the test section. In this way, the particles are mixed into the bulk flow during flow conditions, and a uniform density of particles is delivered to the test article. As observed in Figure 2.2, around 25% of the annular cascade was properly seeded with particles. A sample image of the seeded vane passage, again at 11.3 kg/s and 278 K, is shown below in Figure 2.5. Unlike local seeding, semi-global seeding resulted in uniform particle distribution across the entire window, with distinct and identifiable particles.

The laser used to illuminate the particles for this investigation is a quasi-continuous burst-mode Nd:YAG laser that was custom-built by Slipchenko et al. [15] and produces 150 mJ per pulse at 10 kHz. The fundamental output of this laser is 1064 nm, but the 2<sup>nd</sup> harmonic of 532 nm

was used as this wavelength is in the visible light spectrum, which can be imaged directly by a Photron FASTCAM camera and can be aligned without the use of detector cards. The nominal repetition rates of the laser are 10 and 20 kHz, but it can be modified to achieve a range of rates from 5 kHz to 100 MHz. For all the data sets explored in this paper, a repetition rate of 10 kHz was used with a pulse-burst duration of 10 ms. This frequency was chosen since the max frequency that the FASTCAM can operate at full-frame is 20 kHz and the laser fires two pulses per cycle in doublet mode. The doublets have a set spacing that is timed such that the pulses occur during two separate image frames, so the laser frequency needs to be half the camera frequency for this system.

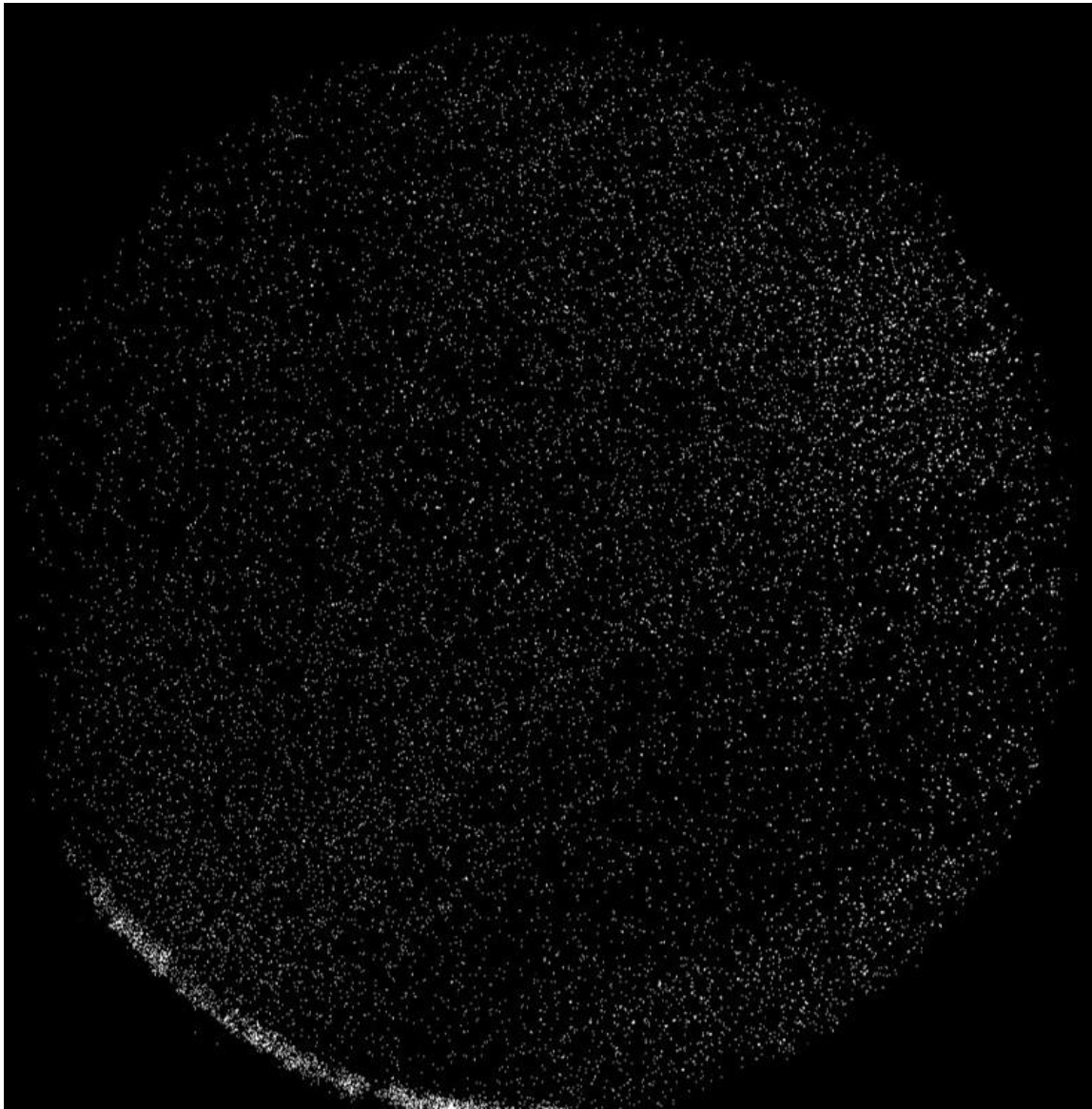


Figure 2.5. Image of illuminated seed particles with semi-global seeding.

## 2.2 Design of Laser Delivery Probe

For the validation of this experimental design, the region of interest is a mid-span cut through the vane passage. This location was chosen as the flow is more uniform and steadier than that of planes nearer to the endwalls, which serves as a more stable target to compare against while troubleshooting the technique. This region also contains large velocity and flow angle gradients, which will test the technique's ability to resolve the flowfield features that are typically used to detect and characterize secondary flows. An example of this plane is illustrated in Figure 2.6, where the interrogation region for the PIV system is circled in red. This region is a result of the intersection between the camera's field of view provided by the optical access holes in the shroud of the vane row and the laser sheet transmitted through the laser delivery probe.

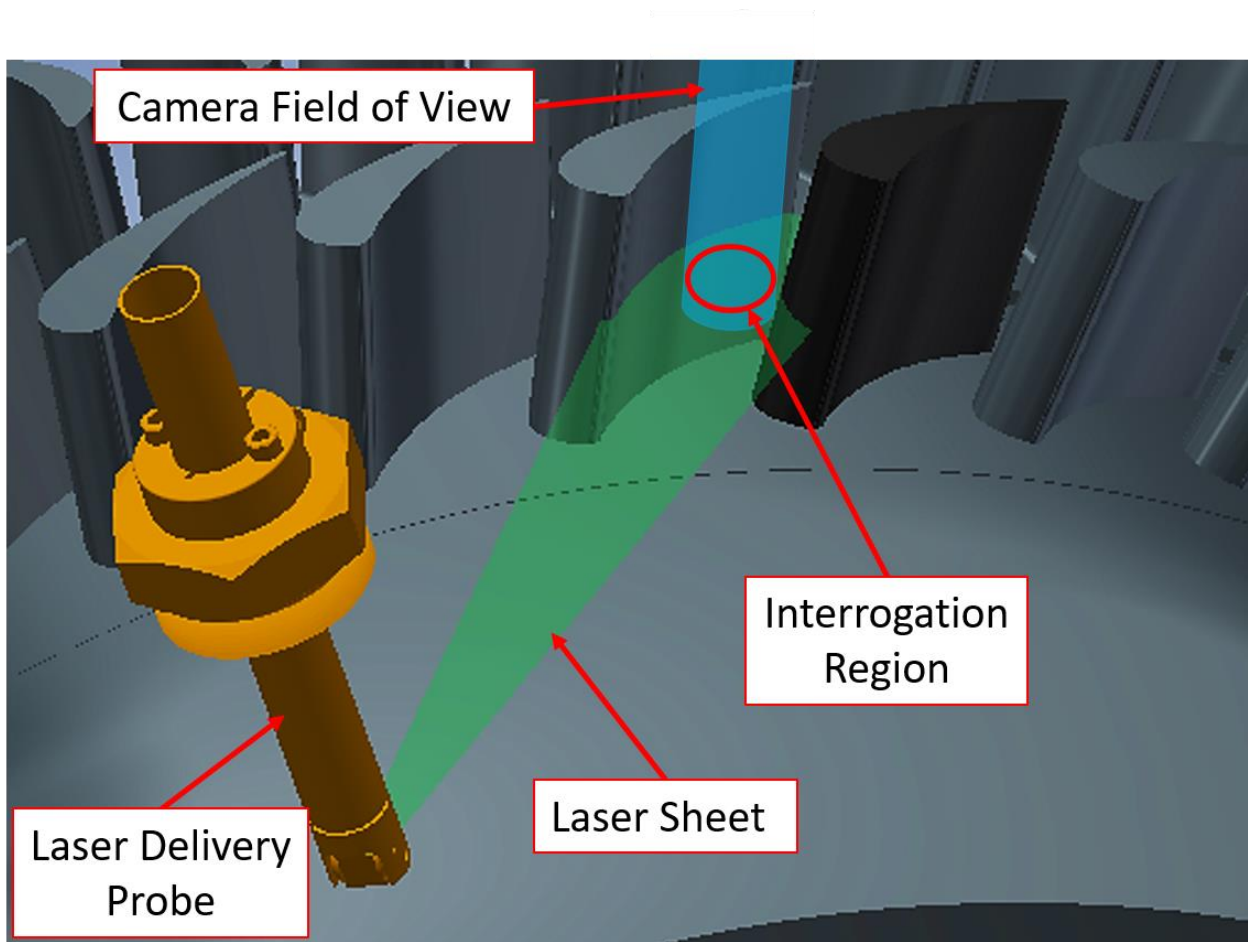


Figure 2.6. Sketch of the method used to deliver the laser sheet into the annular cascade targeting a field of view located at midspan in the passage. The location of the probe avoided perturbations to the flow at the measurement location.

To allow access for a laser sheet in the vane passage, a laser delivery system capable of surviving high temperatures, pressures, and vibrations was designed and built. The design, which is pictured in Figure 2.7, consists of a stainless-steel structure integrated into one of the plugs for the optical access holes that is fixed in place by a shaft collar. A lens tube for 0.5 in. optics is located in the lower portion of the structure to allow for sheet forming optics to be installed within the probe. The configuration shown below has a cylindrical plano-concave (PCV) lens with a negative focal length installed at the bottom of the lens tube and is the configuration used for the majority of the test campaign. Below the lens tube is a permanent window that seals the inside of the probe. Underneath this window is a prism mirror that utilizes a coated hypotenuse to reflect over 98% of the 532 nm wavelength laser pulse (Thorlabs MRA10-K13). The original probe design used a total internal reflection prism, but due to the unconventional geometry of aligning a laser sheet through a vane passage with a high stagger angle in an annulus, it was replaced with the prism mirror to provide more consistent reflectance at non-zero incidence angles.

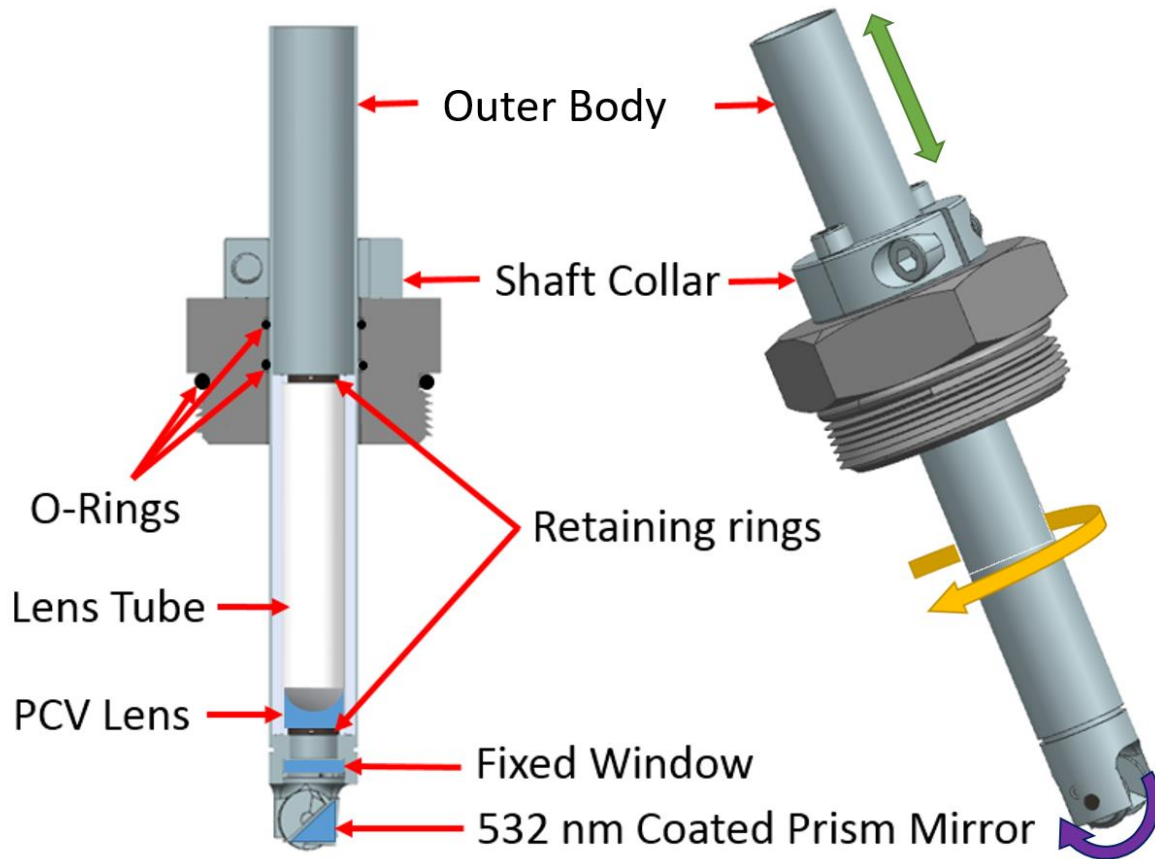


Figure 2.7. Details of the laser delivery probe.

The body of the probe is adjustable in rotation angle and depth as indicated by the yellow and green arrows, respectively, to allow for adjustment of the laser delivery location. A seal is achieved between the probe body and the optical access plug through internal piston O-rings. The shaft collar is tightened to the probe body and bolted to the optical plug to secure the probe after alignment is finalized. The prism mirror at the end of the probe allows the laser to be turned perpendicularly and directed toward the region of interest. This prism mirror is adjustable in pitch, indicated by the purple arrow, giving the laser beam path the final necessary degree of freedom to deliver a laser sheet into the vane passage. Once the prism is in place, set screws retain its position and prevent displacement during testing.

### 2.3 Experimental Methodology

For this research, two different aerodynamically representative conditions were investigated in the wind tunnel facility. The first one, referred to as the cold condition, is obtained by flowing through the cold line (bypassing the heater) such that the flow is expanded from its reservoir conditions. The second condition referred to as the hot condition, combines flow through both the cold and the hot lines, achieving a higher flow total temperature at the test section inlet. These conditions and their main flow parameters within the test section are summarized in Table 2.1.

Table 2.1. Flow parameters for the different measurement conditions. Tt: total temperature; Re: Reynolds number.

<b>Condition</b>	<b>Tt [K] Plane 1</b>	<b>Re/unit length [1/m]</b>	<b>Mach Number Plane 2</b>	<b>Mass flow [kg/s]</b>
<b>Cold</b>	278	$3 \times 10^7$	0.73	11.3
<b>Hot</b>	450	$2.20 \times 10^7$	0.73	11.3

A schematic of the flow path with the test section location is shown in Figure 2.8. The annulus converges down to Plane 1, which is 35%  $C_x$  upstream of the vane leading edge. Plane 2 is located 43%  $C_x$  downstream of the vane trailing edge. Both planes include total temperature and

pressure measurements and static pressure and metal temperature measurements in the hub and shroud endwalls.

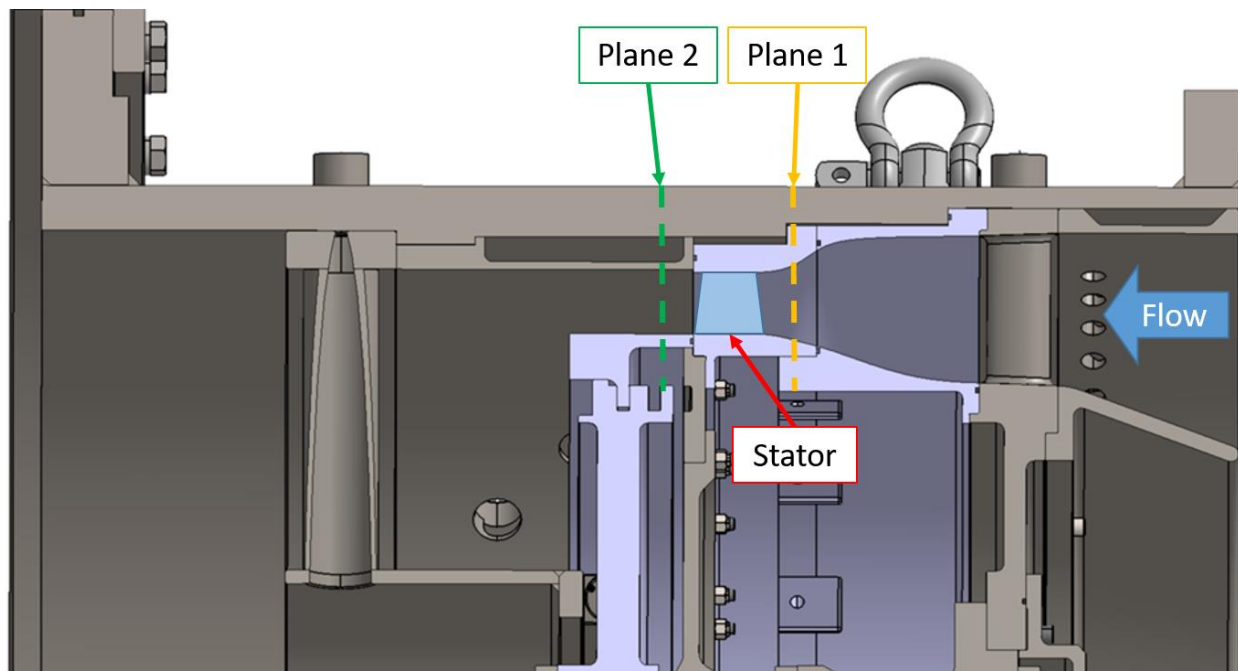


Figure 2.8. Flow path inside the test section and location of the test article.

To produce a laser sheet in the midspan of the first stage vane, the laser is aligned along with a system of optical rails through a positive focal length spherical plano-convex (PCX) lens and into the laser delivery probe. An illustration of this arrangement is presented in Figure 2.9. In the probe, the beam passes through the cylindrical PCV lens, indicated in Figure 2.7, before reflecting off the prism mirror and passing in between the painted vanes of either the vane 1 or vane 2 half of the test article. The PCX lens focuses the beam to a point, while the cylindrical lens spreads the light parallel to the midspan of the vane passage to create a thin sheet passing through the region of interest.

While the laser alignment external to the probe was straightforward, careful alignment procedures were needed within the annular turbine rig where access was limited. A calibrated alignment tool was constructed to provide a reference between the geometry of the rig and overlap of the laser sheet and camera focus location. The alignment tool was set such that it could be inserted through one of the optical access holes and held at the midspan of the first stage vane in view of the camera. The tool contained a calibration grid to focus the camera and create a reference

for relating camera pixels to the real-world reference frame. The tool also contained a target to ensure that the laser sheet would overlap with the focal plane of the camera. Since there was no outside optical access for viewing the location of the laser during alignment, a digital borescope was inserted into the test section to view the laser and make adjustments until the sheet was precisely aligned with the calibration target.

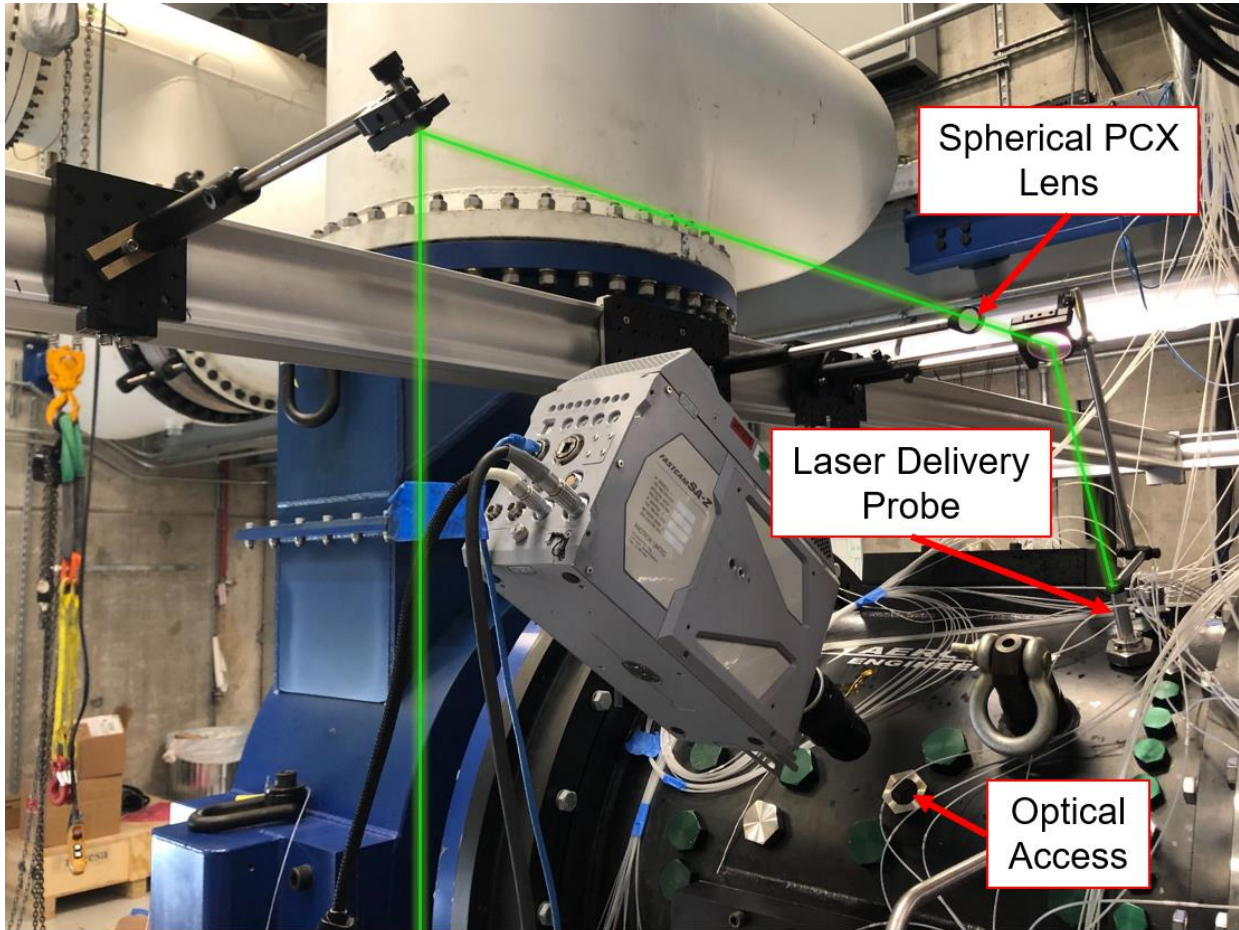


Figure 2.9. PIV setup with camera and laser arrangement in the annular wind tunnel.

Based on a target average particle travel distance between frames of  $\sim 7$  pixels [1] and the expected flow velocity in the region of interest, the required laser pulse doublet spacing for the design mass flow rate in this work is  $\sim 3 \mu\text{s}$ . Given that the camera is operated at 20 kHz for these experiments (i.e., a frame-to-frame temporal spacing of  $50 \mu\text{s}$ ), the frame straddling technique is employed to record images with a very short time spacing. This technique consists of timing the

first laser pulse of each doublet at the end of the exposure of one frame and the second pulse at the beginning of the next frame. The timing scheme, which is controlled by a digital delay pulse generator, is depicted in Figure 2.10. Given that the pulse width of each laser pulse is on the order of 10 nanoseconds, the two images appear to have a time interval equal to the doublet spacing ( $3 \mu\text{s}$  in this case) regardless of the frame rate. As this approach requires two frames per velocity field, the effective velocity field measurement rate is 10 kHz. For a narrower field of view and/or reduced spatial resolution, this same setup can be used with a camera frame rate of 200 kHz to produce PIV data up to 100 kHz. PETAL's custom-built burst-mode laser systems [9] have successfully produced PIV data up to 1 MHz [10] in other experiments.

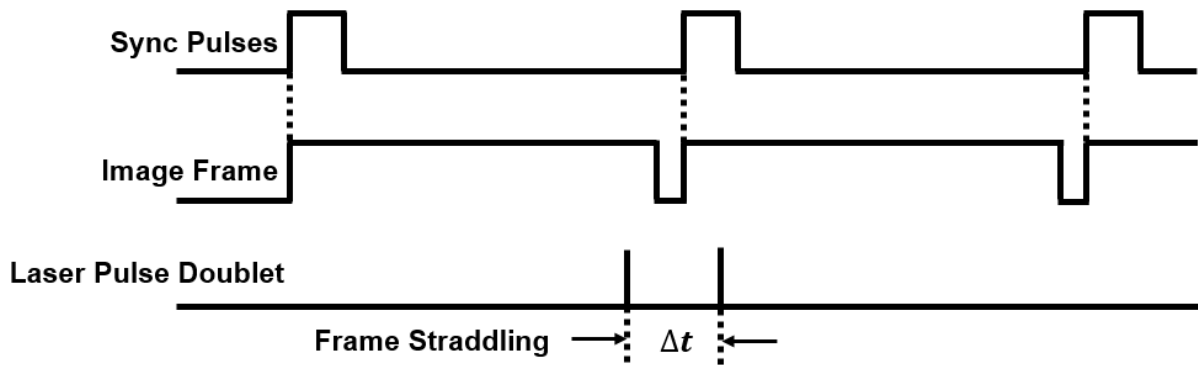


Figure 2.10. Frame straddling scheme.

The measured velocity fields computed using PIV processing algorithms are qualitatively and quantitatively compared to data from Reynolds-averaged Navier-Stokes (RANS) numerical simulations of the same flow geometry and conditions. These simulations were carried out by a postdoctoral researcher of PETAL using the Numeca FINE<sup>TM</sup>/Open solver. The computational domain, shown in the top frame of Figure 2.11, is modeled based on the actual hardware of the annular cascade. One single passage is modeled, composed by a convergent section, a vane row, and a straight section. The unstructured grid, built with Numeca HEXPRESS<sup>TM</sup>, contains approximately 6.5 million elements. The boundary conditions used in the computations are depicted in Figure 2.11. Total pressure and temperature are imposed at the inlet, using the values retrieved from local probes during the experiments. Additionally, flow direction and turbulence quantities,  $k$ , and  $\epsilon$ , are imposed. The static pressure measured with pressure taps is imposed at the hub and extrapolated over the outlet based on radial equilibrium. The passage is modeled using periodic walls, while the solid walls are modeled as isothermal walls based on wall temperature

measured during the experiments. The gas is modeled as real gas, and the  $k-\omega$  SST model is adopted for turbulence closure. Since the simulation was performed on a simplified model of the test section, the results were not fully representative of the complex flowfield within the full wind tunnel.

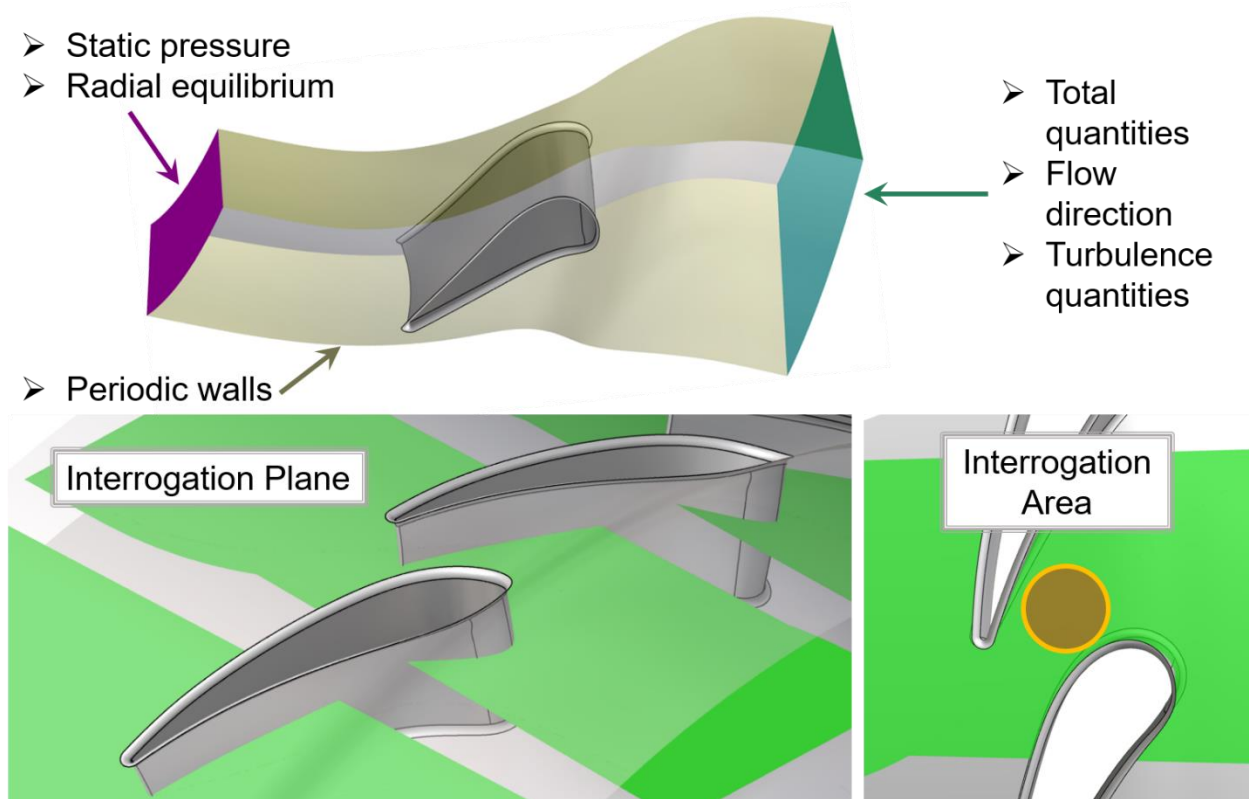


Figure 2.11. CFD computational domain and interrogation areas for PIV-CFD comparison.

The interrogation plane of the PIV is reconstructed into the CFD domain based on the reference location and direction of the laser sheet. The bottom frame in Figure 2.11 highlights the interrogation plane (in green) and area (circled), respectively. Vector quantities are projected onto the plane, and then the flow quantities, including magnitude and direction of the in-plane flow velocity, are extracted for comparison with PIV.

With the region of interest being in the middle of the vane passage, there are no measurements from physical instruments such as hot wire anemometers or pitot-static probes that can be used for direct comparison with the PIV results. However, a circumferential and radial traverse of the vane exit was conducted by other members of the PETAL team using 5-hole probes like the one pictured in Figure 2.12. The probes contain 3 heads to reduce the number of steps

required to traverse the radial span of the vane exit and 5 pressure taps per head to enable flow angle measurements, which are extracted from the spatial distribution of pressure data using a calibration map. The 5-hole probe results are used to validate the CFD at the given test conditions, which is the only form of comparison for the PIV data.

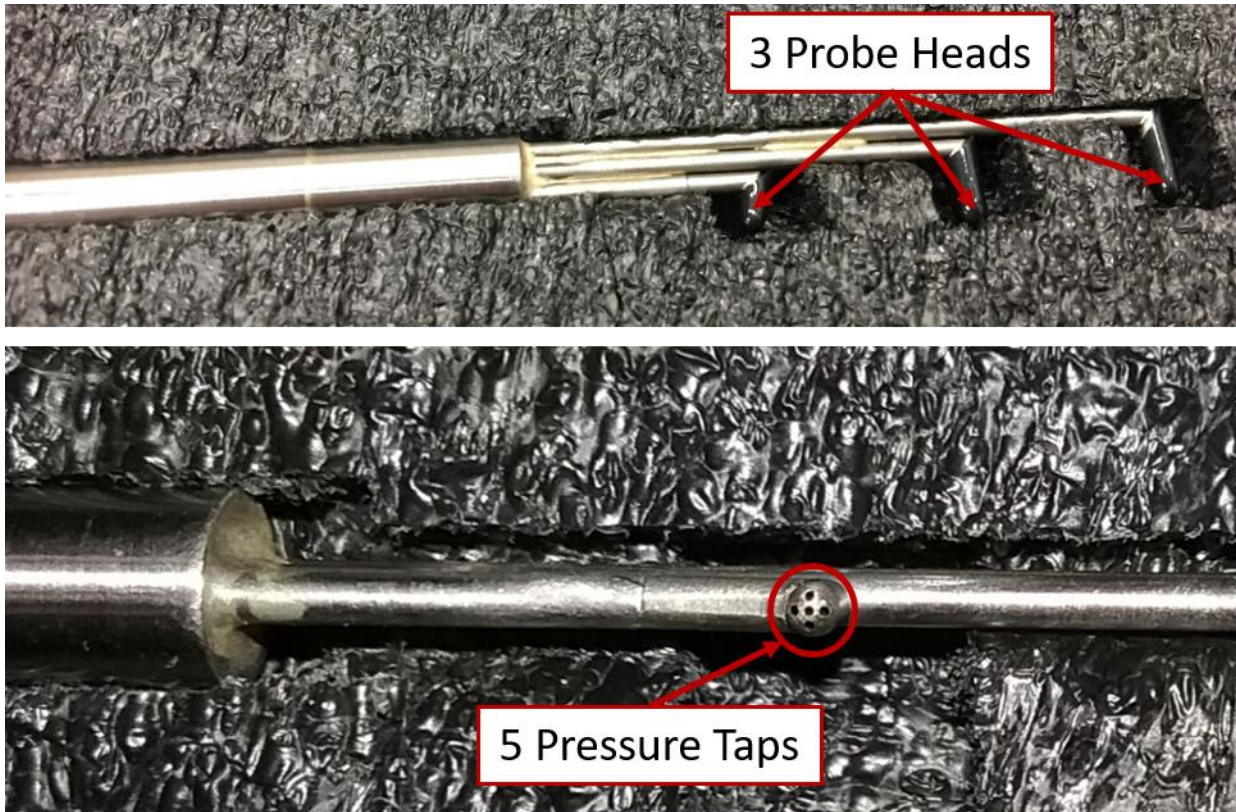


Figure 2.12. Details of the 5-hole probes used in BRASTA.

#### 2.4 Development of Data Processing Tool

To improve the detection of particle movement within the PIV region of interest, a tool was developed in MATLAB to modify the display properties of each individual frame. First, the range of useful images is extracted from each data set based on the presence of the laser in both images of each frame straddling pair. Due to a significant variation in the mean intensity of each frame across a data set, highlighted in Figure 2.13, frame-by-frame background subtraction is performed using images from a no-flow data set and matching each frame to its corresponding image with the flow.

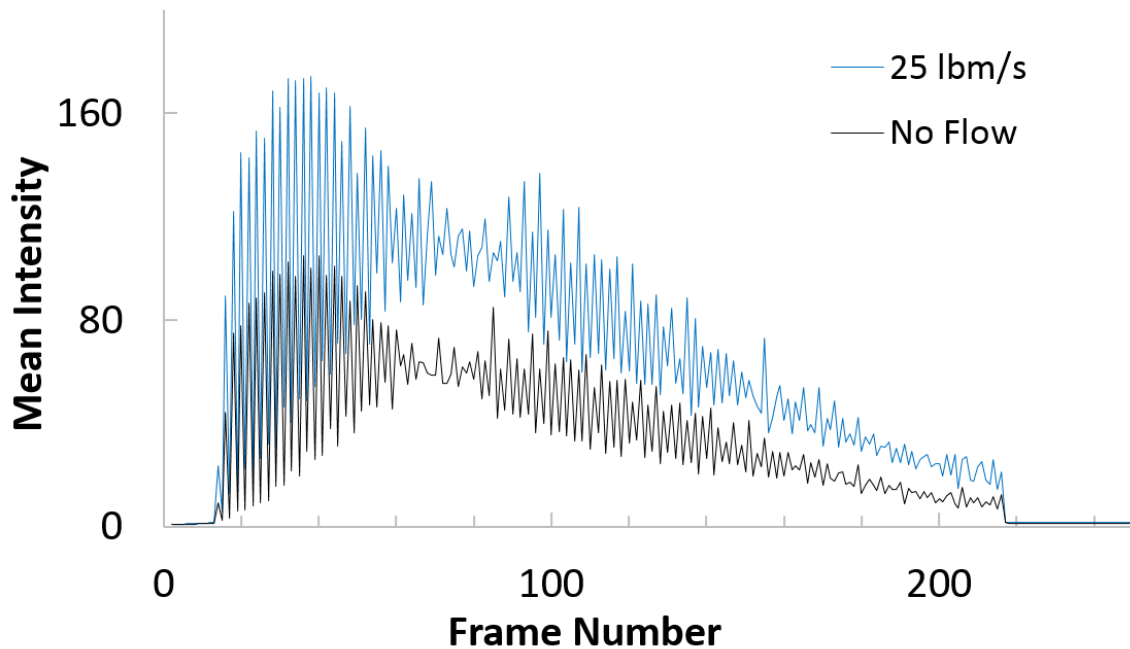


Figure 2.13. Image intensity as a function of the frame number.

To aid in the explanation of the image pre-processing tool, a flowchart of the process can be found in Figure 2.14. After subtracting the background images, a geometric mask is created based on a reference image showing the window outline that bounds the useful data. Next, each image is optimized for the number of centroids (particles) by varying the contrast cutoff level from high to low. The optimization is truncated if camera noise found within a portion of the frame with no particles exceeds a designated limit. For this tool, camera noise is defined as centroids detected by the program that are not seed particles. For the image sets in this study, a corner of the frame outside the optical window was used as this area could never contain seed particles, nor could it be illuminated by the laser pulse or any scattering. If light scattering exists within the region of interest after background subtraction, a second limit is assigned based on the maximum expected number of centroids. Like camera noise, light scattering within the region of interest appears at low contrast cutoff levels and contributes greatly to the number of centroids. Image pairs with low scattering can be used to identify the expected number of centroids for an image set. This limit prevents the data set from being polluted by too many false centroids. After identifying the contrast level that produces the greatest number of centroids for both images in an image pair, if the number of centroids across the pair differs by more than the allowed amount, the contrast cutoff level of

the more centroid-dense image is increased so that the number of observed particles is decreased and the established limit is satisfied. This boundary was added because during the development of this software, it was discovered that when simply maximizing each image's number of centroids, the velocity vector yield was often worse if the two images of a correlation pair greatly differed in number of particles. Lastly, the resulting images are binarized so that the intensity of each particle is normalized. This eliminates any bias created by the differences in mean intensity between the two images in a pair that was highlighted in Figure 2.13.

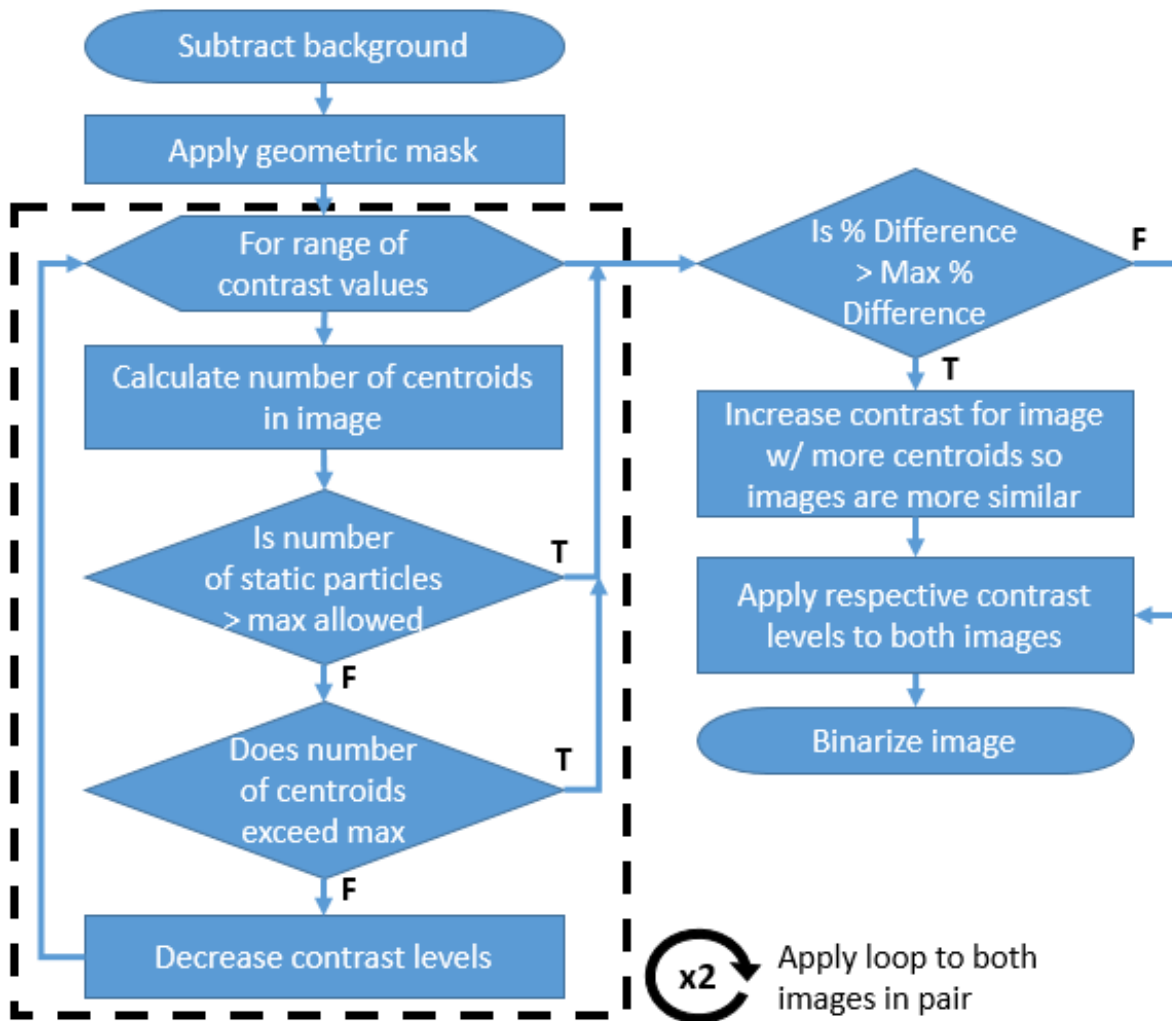


Figure 2.14. Image pre-processing flowchart.

An example of the centroid optimization is shown in Figure 2.15. The plot displays the number of centroids detected by the program as the contrast level is decreased from 500 to 40 for the 31<sup>st</sup> and 32<sup>nd</sup> frames of an image set from the vane 2 configuration at hot test conditions. The

first image, represented by the blue line, does not trigger any of the limits within the optimization loop and thus displays a non-zero value for the entire range. The number of centroids steadily increases with the decreasing contrast limit until it reaches a peak at a contrast limit of approximately 60. After this peak, the number of centroids rapidly decreases until the lower limit of the loop is reached. This decrease is due to the very low contrast levels causing the centroids to increase in size and eventually merge together, effectively decreasing the detected number of particles. The second image, represented by the orange line, triggers one of established limits at a contrast level of 124, below which it displays a value of zero for the remainder of the contrast levels. Fortunately, this limit was triggered after a peak had already been reached at a contrast level of approximately 165. This difference in optimal contrast level across the two images demonstrates the need to enhance the images individually. Unfortunately, the number of maximum centroids for the image pair differs by more than the established max percent difference of 25% for this data set, so a higher contrast level will be applied to the second image such that the final binarized image contains no more than 125% of the number of centroids detected in the final first image.

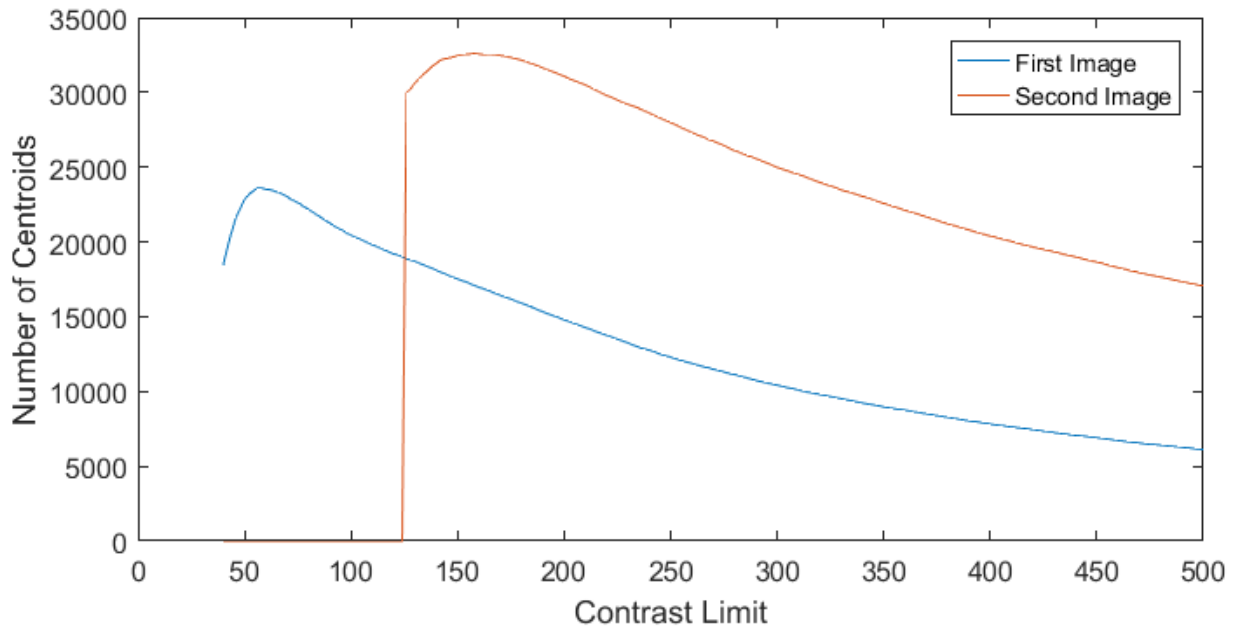


Figure 2.15. Number of centroids detected in image pair (31<sup>st</sup> and 32<sup>nd</sup> frames) as a function of contrast limit from vane2 experiment at hot test conditions.

A second example of the optimization loop is shown in Figure 2.16 to demonstrate an alternative outcome of the image pre-processing tool. For this plot, the first image is the 71<sup>st</sup> frame

of the same data set as before and the second image is correspondingly the 72<sup>nd</sup> frame. Both images in this pair trigger one of the loop exceptions as neither of them reach the lower limit of the loop. However, the percent difference between the two images is less than 25%, so the contrast limits that yielded the max number of centroids for each image are applied to both, respectively, before binarizing the images.

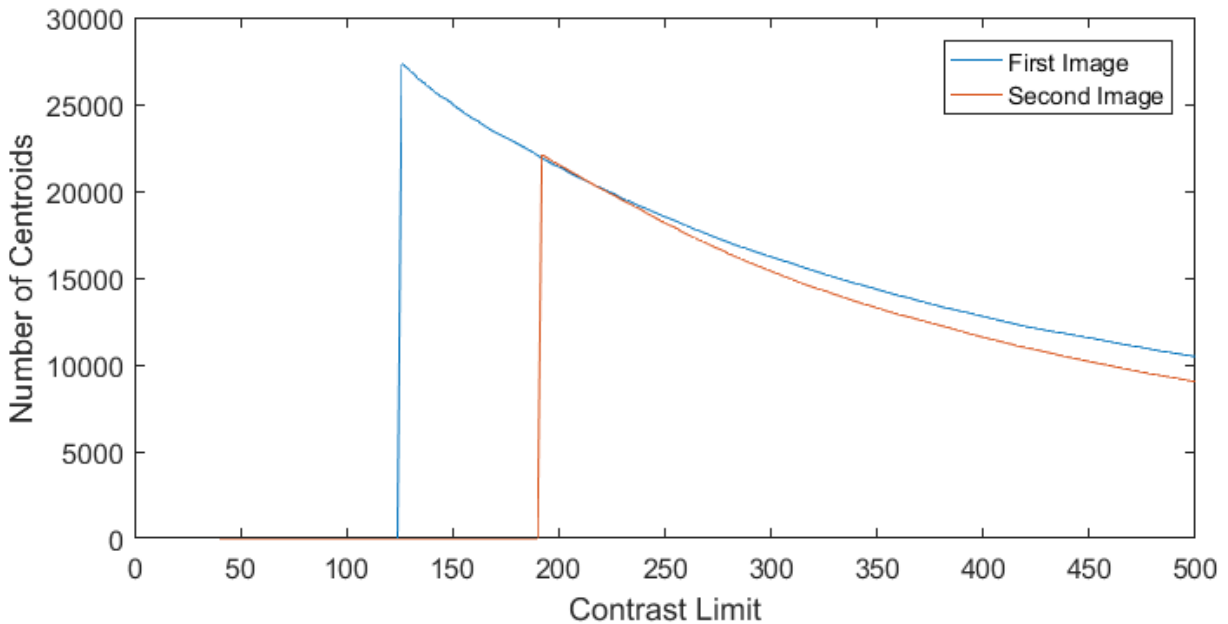


Figure 2.16. Number of centroids detected in image pair (71<sup>st</sup> and 72<sup>nd</sup> frames) as a function of contrast limit from vane2 experiment at hot test conditions.

The enhanced images are then processed in LaVision's DaVis PIV code as a time-series of double frames. Sequential cross-correlation of frame pairs is performed via a multi-pass vector calculation involving 3 passes of a 64x64 pixel square window with 75% overlap, followed by 2 final passes of a 32x32 pixel circular window with 50% overlap. Allowable vector ranges, peak ratios, and universal outlier detection are used to remove outliers, but no vectors were replaced through interpolation to fill or smooth the vector field. The vectors fields were then converted from pixel displacement to velocity based on calibration images of the test article geometry and time spacing between successive laser pulses.

### 3. EVALUATION OF METHODOLOGY IN ANNULAR CASCADE

#### 3.1 First Application of Technique

Because the laser sheet enters the test section at a different circumferential location than the vane passage to align with the stagger angle of the vanes, one of the most difficult aspects of the alignment is matching the angle of the laser sheet with the midspan plane. For the initial experiments, the sheet forming PCV lens was located just outside the laser delivery probe to allow for easier adjustment of the sheet angle. This alternate configuration is depicted in Figure 3.1. The PCV lens is set in a rotating mount, which gives the user the ability to rotate the orientation of the sheet to match the region of interest and align with the test article geometry. This setup configuration was used only for establishing alignment procedures and experimental practices and is presented here to highlight the potential challenges in achieving optimal imaging conditions and the utility of the custom pre-processing algorithms under non-ideal imaging conditions.

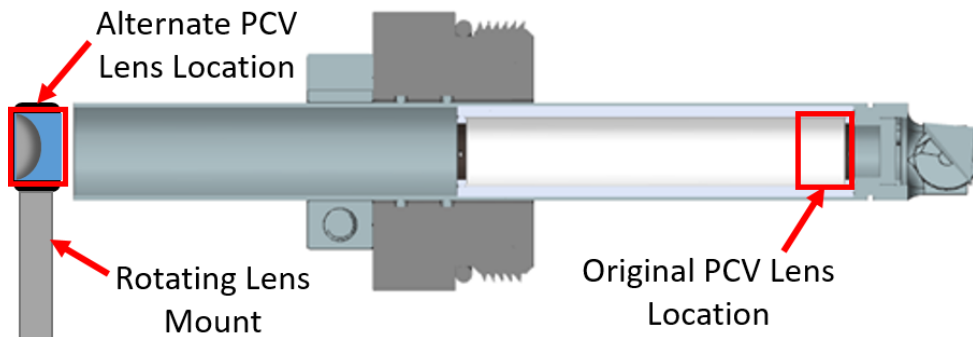


Figure 3.1. Alternate PCV lens location with respect to laser delivery probe.

As a baseline result, velocity fields from the vane 1 configuration at cold test conditions were first computed with only the image pre-processing tools included in the DaVis code. Shown in Figure 3.2A is a time average of all the velocity fields produced from an image set using these tools. Because of the poor image quality, the initial and final correlation window sizes were 128x128 and 64x64, respectively, rather than 64x64 and 32x32, resulting in the relatively few (~100) vectors shown. After applying the image pre-processing techniques to accommodate the variations in signal intensity, as shown previously in Figure 2.13, the number of resolved velocity vectors was greatly increased, totaling closely 1400 vectors with a final interrogation window of 32x32 pixels, as can be seen in Figure 3.2B. Subsequent measurements with improved laser

illumination of the imaged region, described below, achieved further increases in the number of computed vectors.

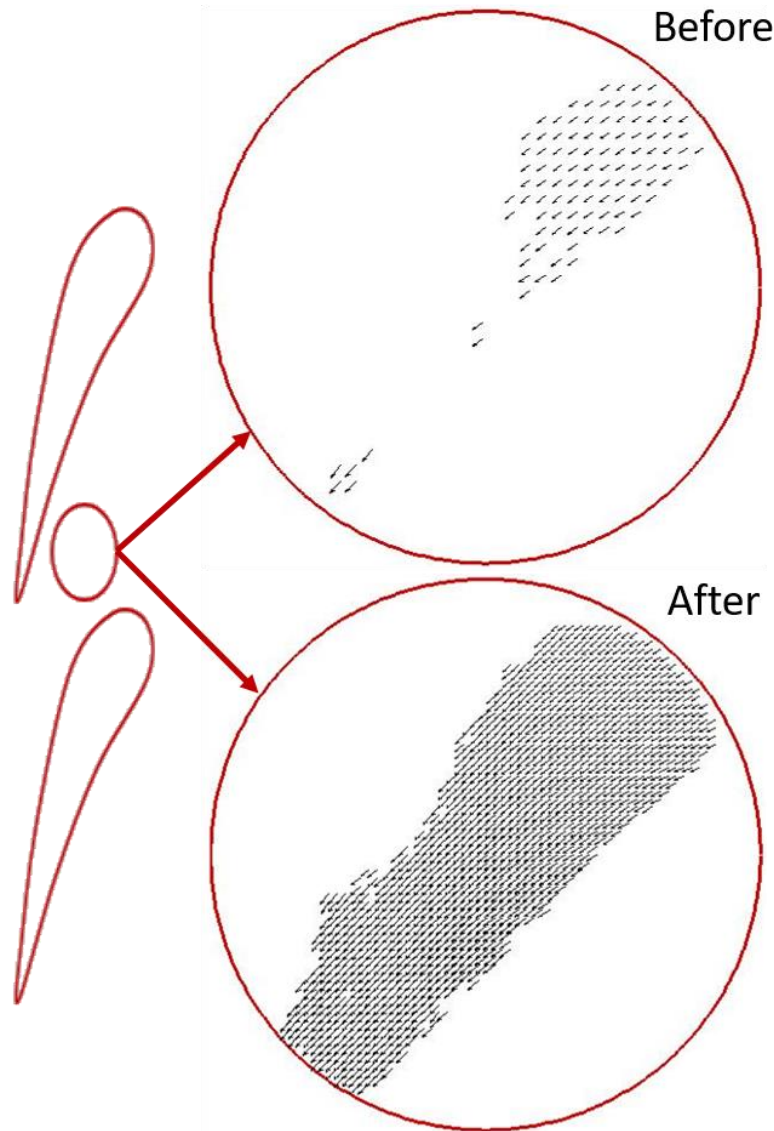


Figure 3.2. Comparison of vector fields (A) before and (B) after implementing custom image pre-processing techniques on the vane 1 experiment at cold conditions.

An inconvenience of this positioning is that the sheet was clipped by the 10 mm prism mirror for the imaging used in the development of the preprocessing procedures. The cause of this was a misalignment in the concentricity between the laser delivery probe and the sheet forming optic. This resulted in a narrower sheet at the region of interest, as can be seen in Figure 3.2 and Figure 3.3. Furthermore, the sheet entered the region from the top right of the circle, and due to a suspected misalignment between the camera and the laser sheet, the particles in the bottom left of

the circle were less resolved. As a result, an even narrower band of velocity vectors were identified by the correlation algorithm. Although this narrow band of velocity data restricts the analysis of the flowfield, the velocity contour and streamlines presented in Figure 3.3 confirm that the high velocity gradient within the passage is being captured and that the seed particles are following the high curvature of the vane profile.

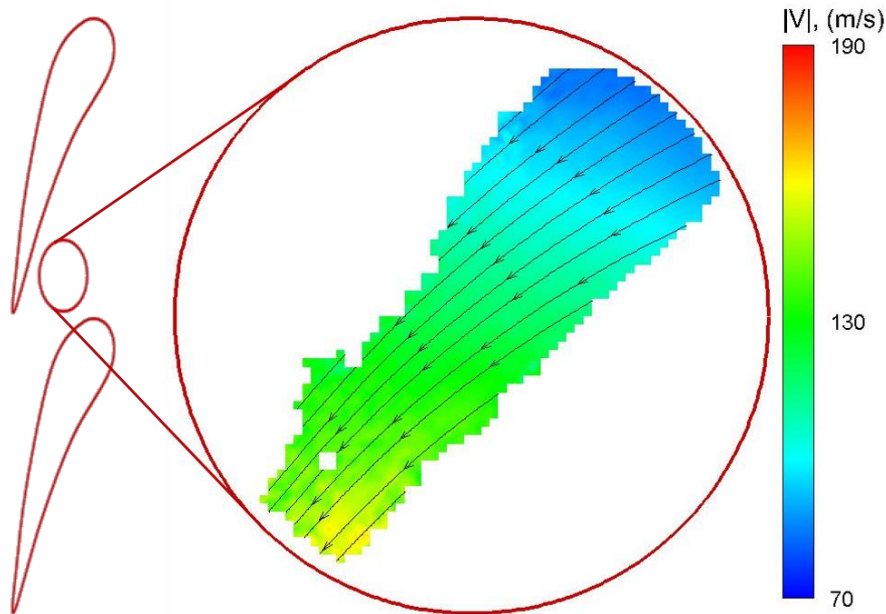


Figure 3.3. Time-averaged velocity contour in a preliminary evaluation of the flow of the vane1 experiment at cold test conditions with streamlines.

To verify that the cross-correlation program was accurately resolving the velocities from the image pairs, the correlation maps of one of the instantaneous velocity fields from vane1 image set used in Figure 3.3 were evaluated. Figure 3.4 displays the velocity field on the left along with a red box highlighting the vector location for the correlation map shown on the right. The 3D map illustrates the correlation value of the pixel window with respect to the displaced location. The origin is the location that the program identified as the correct displacement, which is why a peak with a maximum correlation value of 1 exists at this point. The surrounding points are the correlation values for the window if it was displaced by the indicated number of pixels away from the estimated location. As there are no large peaks beyond the origin and the PPM is greater than 5, this correlation map indicates that the program is able to extract particle displacements with certainty. Moreover, the narrow width of the center peak is a good indication of precision in the estimation of the true displacement. This is only a qualitative assessment of the uncertainty of the

measurement technique, but it is enough to justify the application of the methodology to the vane2 configuration.

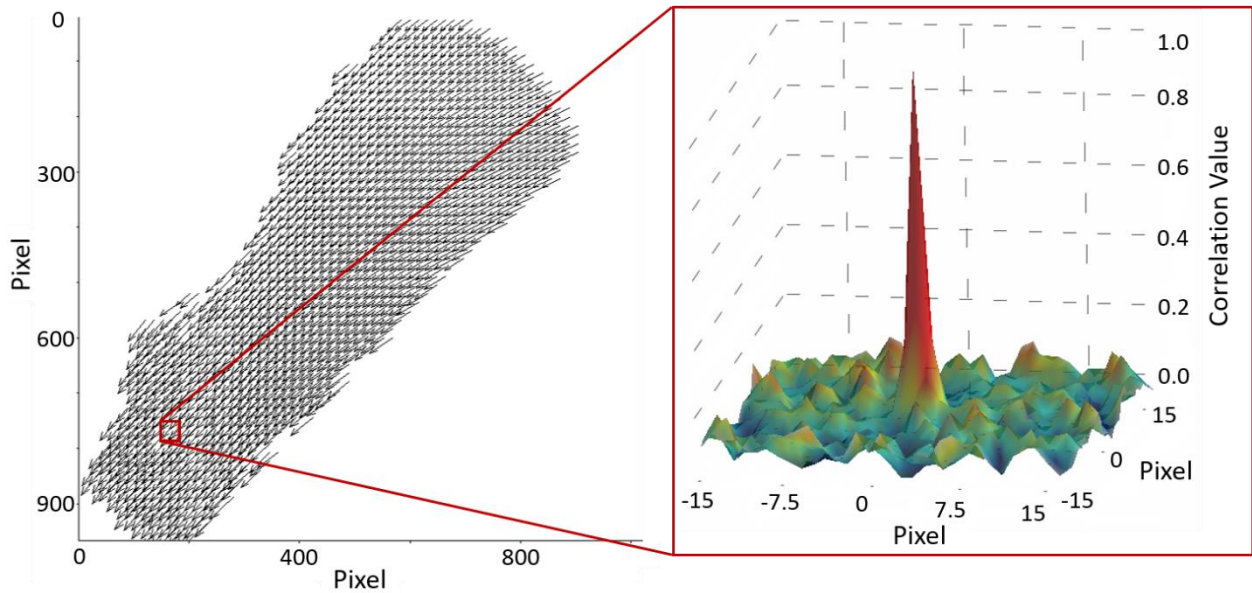


Figure 3.4. Correlation map for a velocity vector from vane1 configuration at cold test conditions.

After the development of laser alignment procedures, the PCV lens was moved back into the laser delivery probe to its original design position. In this location, adjustment of the PCV lens orientation becomes more difficult, but the proximity to the prism mirror prevents the clipping shown above and allows the laser sheet to span the entire width of the interrogation region.

### 3.2 Time-Averaged Flowfield Analysis

The following flowfield analysis is based on 101 averaged PIV vector fields of the vane2 configuration and compared to the CFD results for both the cold and hot-gas experiments. Figure 3.5A and B show the contours of in-plane velocity magnitude in the interrogation area for PIV and CFD, respectively. The same color bar is used for both contour fields, with a minimum of 70 m/s to a maximum of 190 m/s. The PIV measurements show a monotonic increase in the velocity from the top of the domain to the bottom, which is consistent with the expected flow acceleration through the stator row. A similar trend can be observed in the CFD results. Since the interrogation area is in the middle of the passage, as depicted in the sketch in Figure 3.5, the top section of the circle lays close to the pressure side near the trailing edge, while the bottom portion of the circle is located close to the front suction side of the adjacent airfoil. Hence, the observed velocity

gradient is consistent with the velocity difference usually existing between the pressure and suction side. While the velocity profiles are similar for the measured and computed velocity fields, the mean velocity appears to be higher in the CFD calculations. Even though the PIV maybe matching the trend of Mach number, which is generally well-predicted by CFD, the slight mismatch in the magnitude of velocity can be due to a difference between the temperature considered for CFD versus the experimental case.

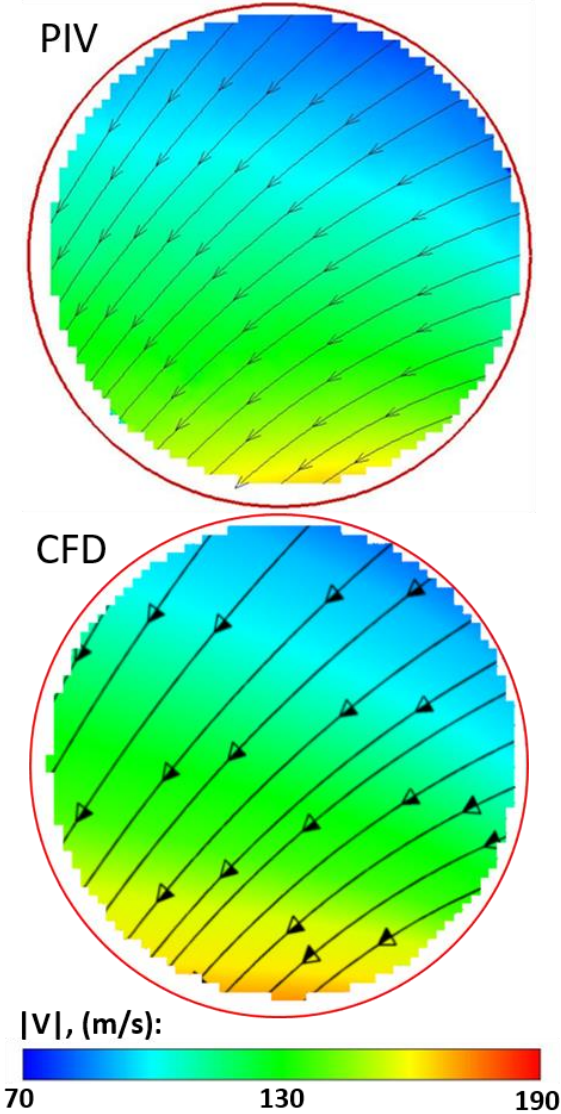


Figure 3.5. Time-averaged velocity contour of the flow of the vane2 experiment at cold test conditions with streamlines from (A) experimental measurements and (B) CFD model predictions.

An assessment of the flow topology can also be made based on the direction of the streamlines. These lines appear to be rather straight on the top-left quarter of the measured region,

while towards the bottom right quarter the streamlines have a notable curvature. This is due to the presence of the more significant wall curvature in the front portion of the suction side. These qualitative features, found both experimentally and numerically, can be further verified by comparing the flow angle. Figure 3.6 shows the contours of the tangential flow angle. The experimental and CFD data show good agreement in terms of the time-averaged values and spatial distribution of the flow angles. As it is observed in the contour plots, the turning is slightly higher in the CFD prediction, but not exceeding the measured  $70^\circ$  angle in the trailing edge zone.

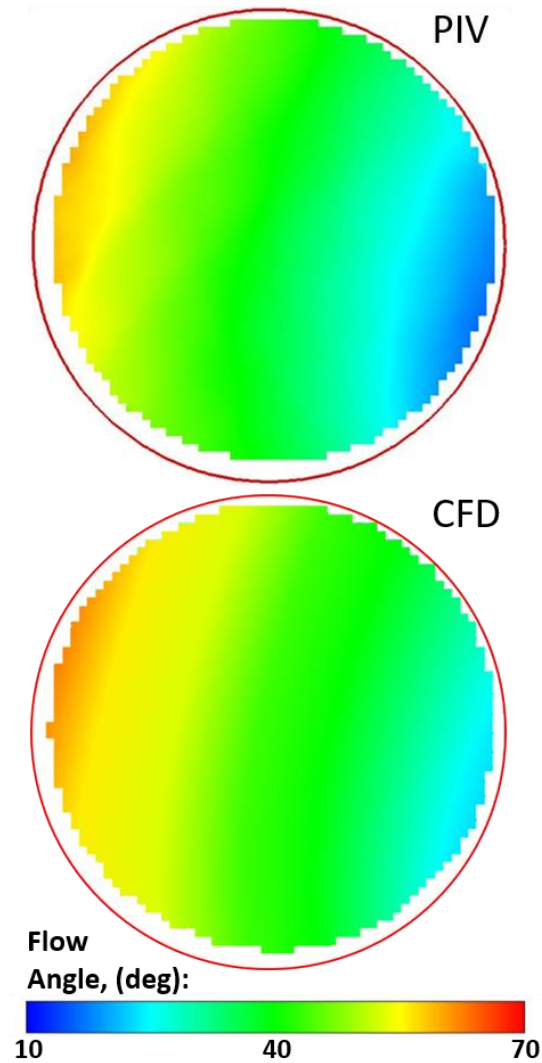


Figure 3.6. Time-averaged flow angle contour of the flow of the vane2 experiment at cold test conditions from (A) experimental measurements and (B) CFD model predictions.

In the hot experimental conditions, higher velocities are observed than in the cold conditions, as expected, with the average measured velocities being slightly less than CFD

predictions. The lower measured velocities in both cases could be an indication that the seed particles are not fully tracking the flow, a phenomenon known as particle lag. For the results shown in Figure 3.7, the low velocity patch in the top right corner may be due in part to the scattering of light from inside the rig.

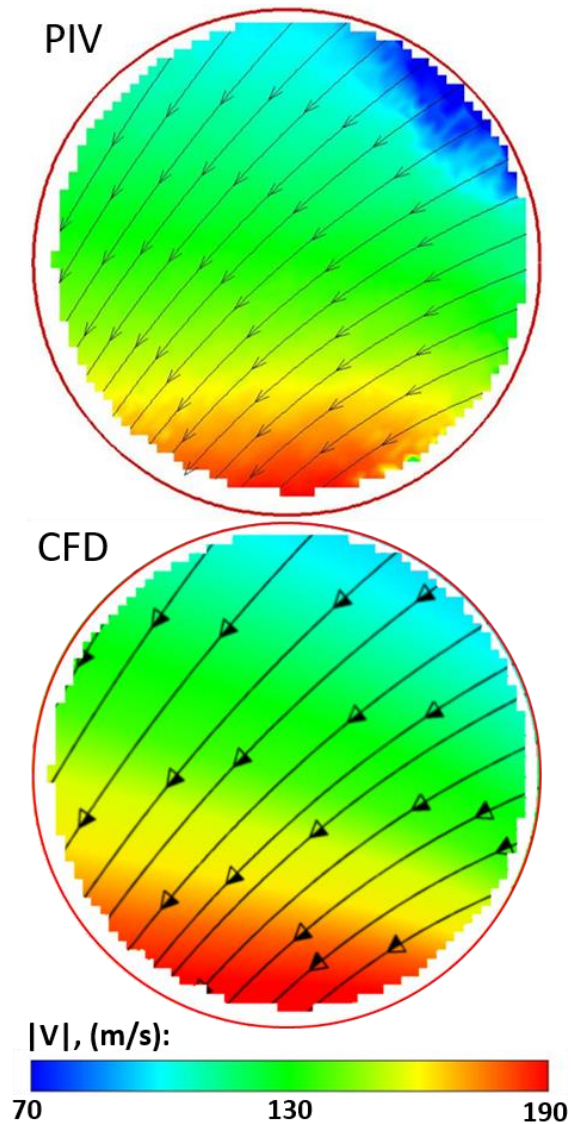


Figure 3.7. Time-averaged velocity contour of the flow of the vane2 experiment at hot test conditions with streamlines from (A) experimental measurements and (B) CFD model predictions.

Due to the harsh conditions of testing, small deposits began to form on the internal probe optics during the hot experiments, which were performed last, as a result of the gradual erosion of a paint coating on the lens tube inside the laser delivery probe. These deposits produced scattering that enters the rig with a different trajectory than the primary laser sheet. Given that the interior of

the test section is polished aluminum, stray beams of light are susceptible to reflecting into the camera's field of view. Based on a qualitative assessment of the unprocessed images, some of this scattering intersected with the top right portion of the optical window and obscured the particle movement. It is also possible that the Cerakote ceramic paint deteriorated over time and contributed to this scattering; however, a visual inspection of the vane passage did not yield any evidence of erosion. As in the case of the cold experiment, CFD and PIV velocities near the suction side are again more alike than in the pressure side.

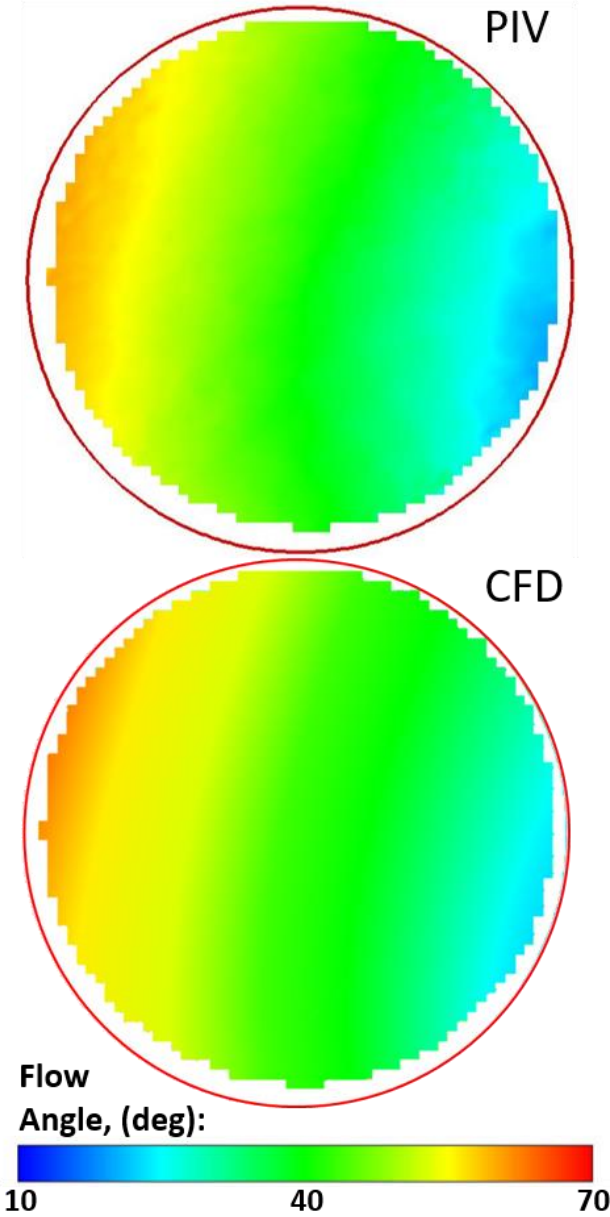


Figure 3.8. Time-averaged flow angle contour of the flow of the vane2 experiment at hot test conditions from (A) experimental measurements and (B) CFD model predictions.

The flow turning angles are similar in magnitude for both the hot and cold flow conditions, as indicated by the measured and computed streamlines. This is anticipated because the temperature affects velocity more so than it affects the flow angle. The light scattering noted in the top right region of the flow does not seem to have a significant effect on the measured flow angle. As observed in Figure 3.8, there is again good agreement between the time-averaged flow angles retrieved with the PIV measurements and the CFD predictions. Both have almost the same minimum and maximum flow angles from  $10^\circ$  at the inlet of the region of interest to  $70^\circ$  at the exit, respectively, close to the trailing edge at the pressure side of the vane. The CFD flow angle gradients appear to be more gradual from the suction side to the pressure side, as indicated by the larger yellow band.

The flow angle was also checked at the exit of the stator with a 5-hole probe. As observed in Figure 3.9, the CFD prediction is within  $1^\circ$  of the measured exit flow angles retrieved by the 5-hole probe at two points in the middle of the passage  $2.2^\circ$  apart. The agreement between the flow angles predicted by CFD and the 5-hole probe and between CFD and the PIV measurements provides strong evidence that the actual flow angles are correctly ascertained within the vane passage.

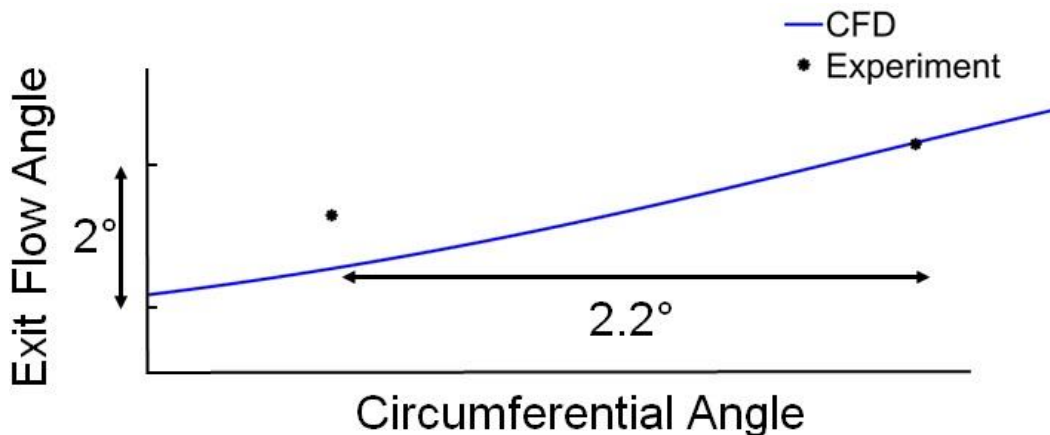


Figure 3.9. Comparison of the flow exit angle at the middle of the passage measured with a 5-hole probe and the CFD prediction.

### 3.3 Assessment of High-Frequency Capabilities

The frame straddling technique produces time resolved data at 10 kHz with a camera frame rate of 20 kHz. A time series of flow angle contours for the vane2 configuration at cold test

conditions is depicted in Figure 3.10. Given that the region of interest was selected for its steadiness, there is little expected variation between frames. In this series of 6 time-steps, the flow angle is nearly constant apart from minor fluctuations near the PS and SS of the window. Furthermore, there are no unexpected structures present in any of velocity fields. The resolution of the vectors in this set could be further improved by increasing the window size, but it comes at the cost of decreased spatial resolution. These cold test results demonstrate that the current optical diagnostic setup can acquire high-frequency velocity measurements of a turbine flowfield.

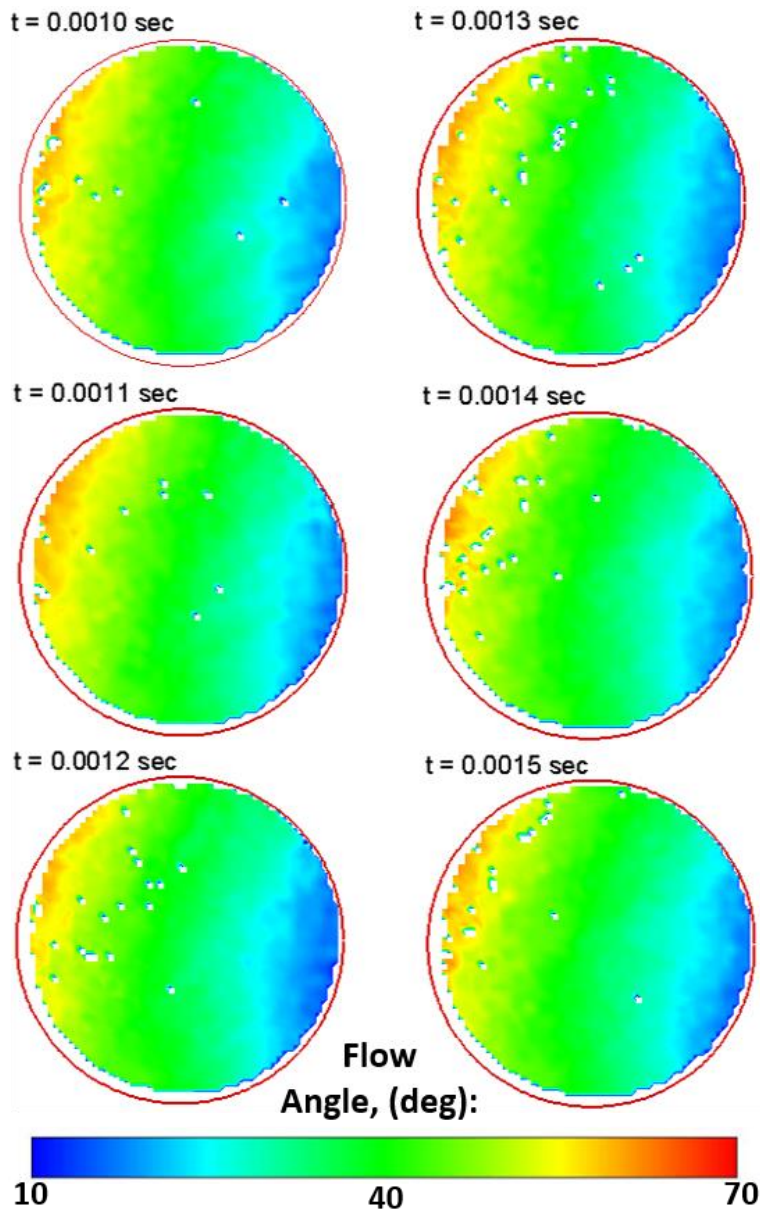


Figure 3.10. Flow angle time series of vane2 configuration at cold test conditions.

One of the barriers to achieving time-resolved PIV measurements is an inconsistency in the vector yield across consecutive correlated image pairs. For both the cold and hot test conditions, the total number of velocity vectors resolved at each grid point including all the data from a set of 101 velocity images is plotted in Figure 3.11.

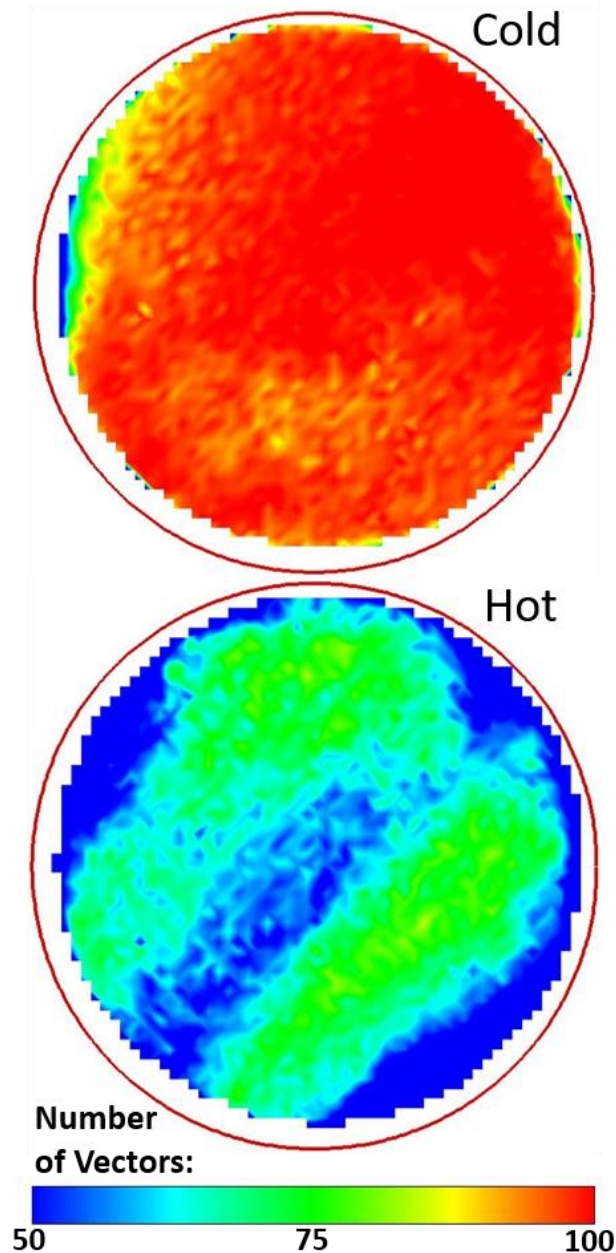


Figure 3.11. The number of vectors calculated across a single image set of the vane2 configuration at (A) cold and (B) hot test conditions.

The cold test case in Figure 3.11A shows that the PIV processing algorithm can produce a velocity vector at nearly all times and across nearly the entire measured region. The edges of the

measured region are expected to be less consistent because of the possibility of losing a particle's initial or final position in an image pair. The areas with computed vectors of 80 or less indicate that the intensity of the laser sheet was too weak in that region to illuminate the particles in some of the frames. As the sheet is expanded from a Gaussian beam profile, the sheet profile was similarly Gaussian in intensity. Due to the setup constraints from the annular geometry, the sheet had a limited distance to expand so the lower intensity tails of the Gaussian profile persist at the edges of the sheet within the vane passage. As the laser sheet is delivered diagonally across the region from top-right to bottom-left, the top-left and bottom-right portions of the interrogation region are at risk of lower particle illumination.

Figure 3.11B shows that the vector yield is lower for the hot test conditions. This may be due to lower particle number densities or the scattering interferences noted earlier. However, an anomalous dip in the vector yield is observed in the center of the measured region where one would expect relatively ideal imaging conditions. One possible cause is that there is a non-uniform illumination of the vane passage between images. The pre-processing code enhances the image based on the particle resolution across the entire frame, so the quality of some regions may be decreased in order to improve the image as a whole. The images are optimized for the surrounding lower intensity particles, which can cause the apparent size of the higher intensity particles to be increased. This distortion of the particles can be significant enough to prevent the correlation software from determining their displacement. To improve the vector yield, the pre-processing code would need to be modified to enhance images by regions as opposed to the entire frame; however, this will greatly increase the computation cost of the tool.

### **3.4 Uncertainty Analysis**

According to Sciacchitano [18], the effects of all the sources of error are fundamentally captured in the acquired images. Even so, not all the error sources can be quantified during the correlation process. Most of these are systematic errors and they include “tracer particle response, hardware timing and synchronization, perspective errors, and calibration errors” [18]. To minimize some of these errors such as the perspective and calibration errors, LaVision employs a self-calibration routine and a series of sub-pixel interpolation and correlation peak-finding routines [19]. Still, many of the uncertainty sources are quantifiable such as “particle image size and shape, camera noise, seeding density, illumination intensity variation, particle motion and image

interrogation” [18]. LaVision calculates the uncertainty from these remaining sources using a correlation statistics-based method that analysis each pixel’s contribution to the shape of the cross-correlation peak to produce a displacement error [19].

To evaluate this error contribution, the pixel displacement error was extracted from the DaVis software and converted to velocity. This velocity error was then averaged across all the frames of a vector time series and normalized using the average velocity for each respective vector grid point. A contour of the percent uncertainty for the vane2 configuration at cold test conditions is shown in Figure 3.12. For the majority of the interrogation region, this bias error results in an uncertainty of less than 1% with an average for the entire region of 1.5%; however, in the bottom-left portion of the window, there is a small region with a peak uncertainty of 6%. Upon inspection of the raw images, there appears to be a spike in particle illumination in this region across a third of the image set. This intensity spike could be the result of a few factors such as variations in the beam profile, laser drift, scattering within the vane passage, or oil depositing on the window and would result in less certain tracking of the particles across image pairs

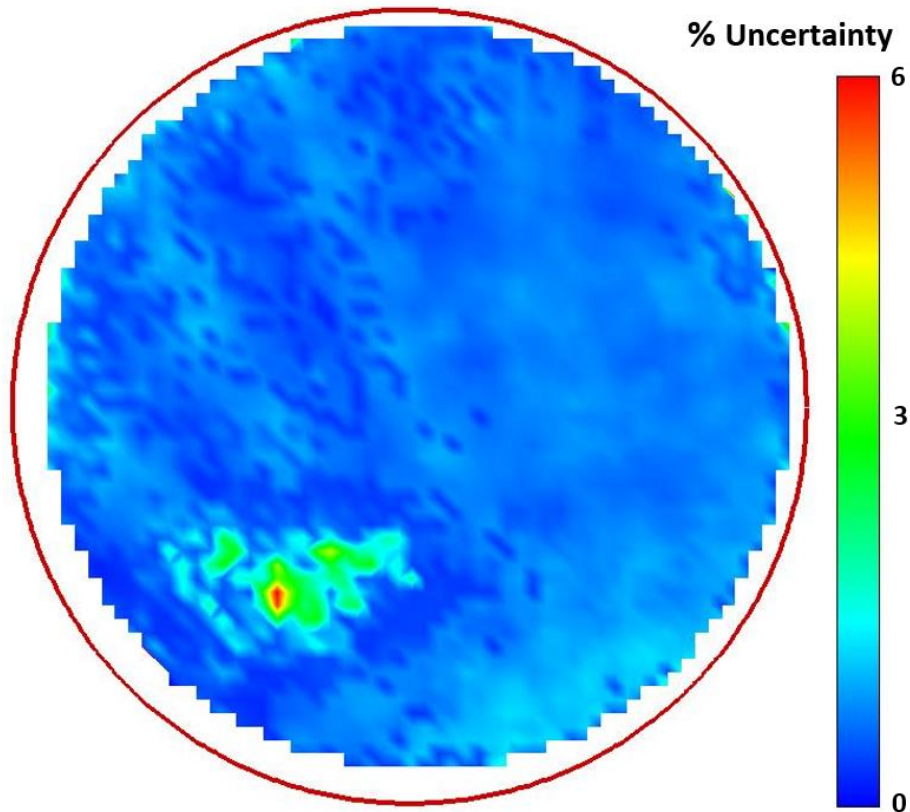


Figure 3.12. Percent uncertainty from correlation bias error for a vector time series of the vane2 configuration at cold conditions.

After reviewing the sample standard deviation of the velocities across the set, reproduced in Figure 3.13, it was discovered that the region of peak uncertainty is collocated with a region of unsteadiness in the velocity field. This variability could be due to true fluctuations in the assumed steady region or the result of the low repeatability with the intensity spike, but it is clear that the increase in uncertainty shown in the previous figure is a consequence of increased precision error as opposed to bias error.

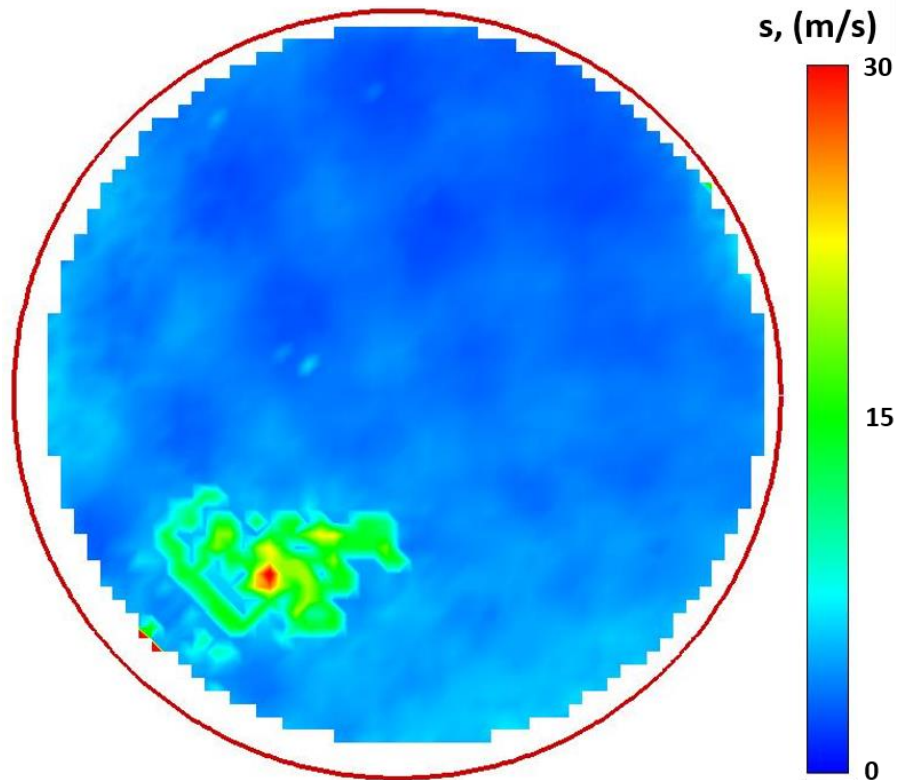


Figure 3.13. Sample standard deviation from vector time series of vane2 configuration at cold conditions.

## 4. DEVELOPMENT OF OPTICAL SETUP FOR TIP FLOW MEASUREMENTS

To facilitate the assessment of the tip flow control designs, a modular two-stage rotating turbine rig was developed by the PETAL team. A layout of the module installed in the high-pressure facility used for BRASTA is shown in Figure 4.1. A motor coupled with a dynamometer is attached to the shaft of the rig to allow for rotation of up to 15,000 rpm and high precision torque measurements to support the determination of turbine efficiency. To aid in the evaluation of the novel tip designs, an optical setup has been designed that adapts the evaluated methodology from 2D to 3D velocity measurements and allows the technique to be implemented in an even more optically restricted environment.

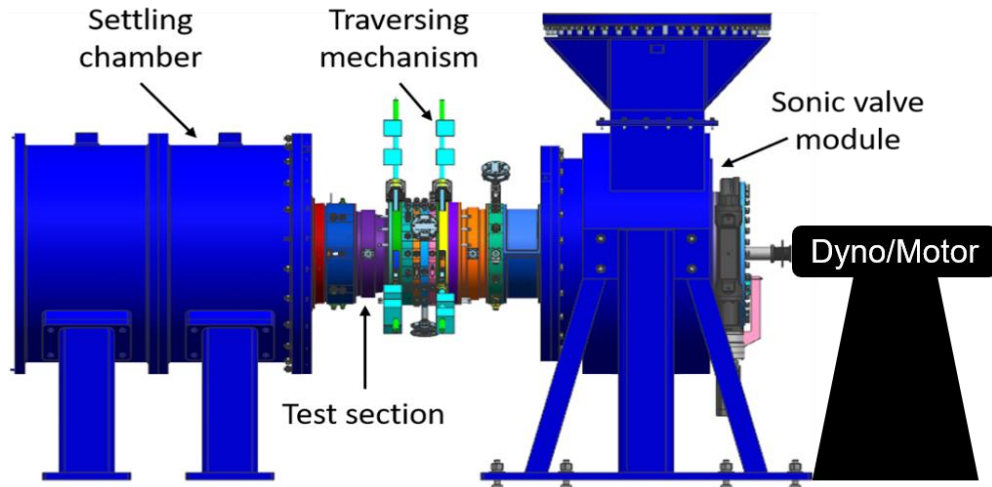


Figure 4.1. Configuration of STARR turbine module.

Endoscopic PIV is a critical technique for STARR because it is a smaller rig, so direct optical access is even more limited than that of BRASTA. The only two forms of access in STARR are small oval openings directly over the blades of the 1<sup>st</sup> and 2<sup>nd</sup> stages, and two traverse rings with circular ports that are located upstream of the 1<sup>st</sup> stage vanes and downstream of the last installed stage. Figure 4.2 provides a rendering of an endoscopic SPIV configuration that makes use of the over blade access for delivery of the laser sheet and a traverse ring downstream of the blades for the placement of two borescopes. The borescopes are circumferentially spaced so that they have overlapping fields of view in plane with the laser sheet, while maximizing their angle of

separation to allow for the implementation of SPIV. The limiting factor is the stagger angle and spacing of the blades. The thickness of the laser sheet will be increased in comparison to the measurements taken parallel to the flow direction to ensure particles are retained in the sheet between image frame as the particles are travelling normal to the laser plane. Based on the average flow velocity within the plane of interest, the thickness of the laser sheet will be chosen such that the average particle movement between laser pulses is less than 30% of the laser sheet thickness, the limit imposed by [6].

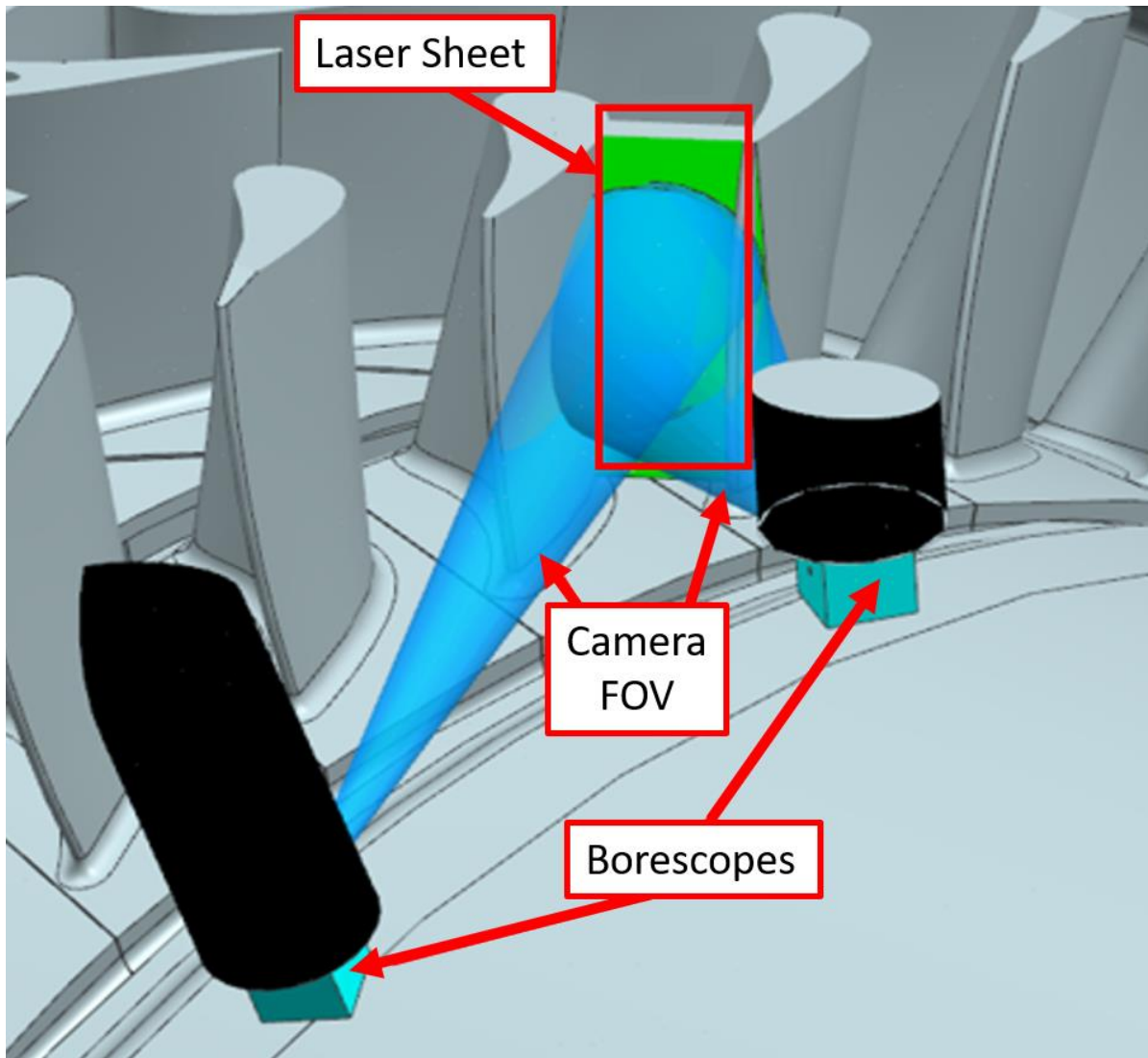


Figure 4.2. Sketch of the proposed method to deliver the laser sheet into STARR and image the rotor passage with two borescopes to perform SPIV.

#### 4.1 Development of Endoscopic PIV in Annular Environment

Having established an experimental procedure for conducting PIV in an annular test section, endoscopic PIV will first be implemented in BRASTA for appraisal. To investigate the secondary flows that are fundamental to managing blade and vane loss mechanisms, the most prioritized planes of interest are those that span radially and capture flow interactions with the endwalls and their boundary layers. A primary plane of interest concerns the study of the HSV saddle point on the leading edge of a 1<sup>st</sup> stage vane in BRASTA. With the discovery of the unsteadiness of the HSV formation, time-resolved high-frequency PIV of a radial plane intersecting the leading edge of the stator would aid in the understanding of this unsteady phenomenon and contribute towards the possibility of controlling it.

The primary difficulty with pursuing this plane of interest is that optical access does not exist on BRASTA that would allow for a camera to capture this region directly. For this reason, the camera needs to be coupled to a borescope so that endoscopic PIV can be performed. A configuration of the laser sheet and borescope that would allow for the HSV formation to be imaged is presented in Figure 4.3. The left image illustrates the circumferential position of the laser delivery probe and borescope required to achieve a perpendicular intersection of the laser sheet and camera viewing plane on the leading edge of a vane. The right image highlights this intersection and portrays the field of view available to the camera from the borescope.

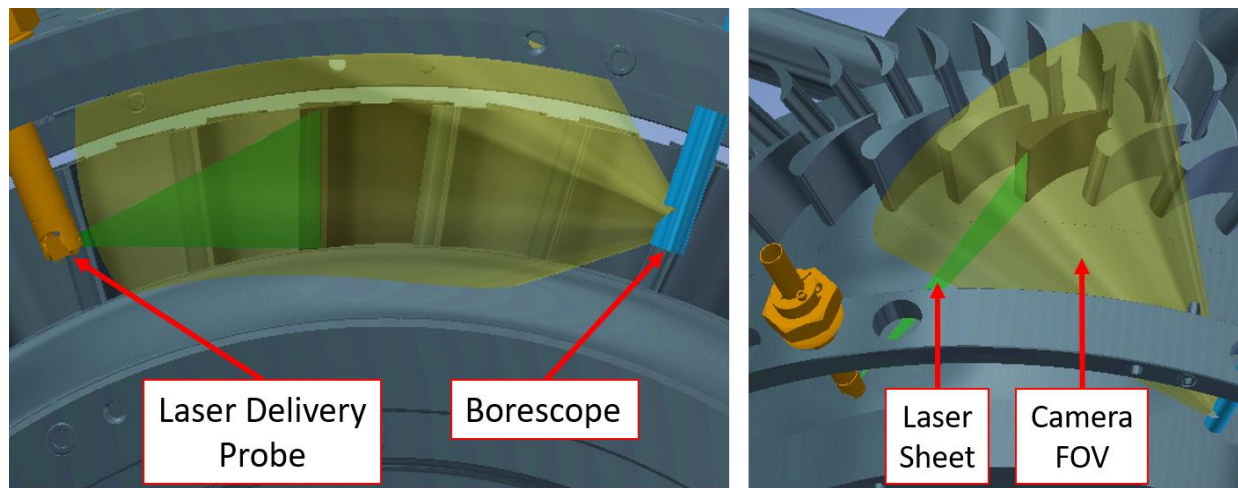


Figure 4.3. Laser and camera configuration for endoscopic PIV in BRASTA.

Due to the adjustability of the laser delivery probe, it can be directly applied to this configuration; however, the borescope and its mounting system needed to be purchased or machined. To survive the harsh testing conditions of the aerodynamically engine representative facility, a custom high-temperature borescope capable of withstanding up to 300° C and 10 bar was purchased from Gradient Lens Corp. (PH07-NVK/Hi Temp). To hold this borescope securely in position, while still providing several degrees of freedom, a mount was designed and manufactured based on the laser delivery probe. Similarly, it features a shaft collar to secure the borescope during testing but allow for axial and rotational movement during alignment as indicated by the green and yellow arrows, respectively. This design has been vacuum-tested and implemented in the collection of high-speed PSP measurements on the surface of the trailing edge of the 1<sup>st</sup> stage vanes.

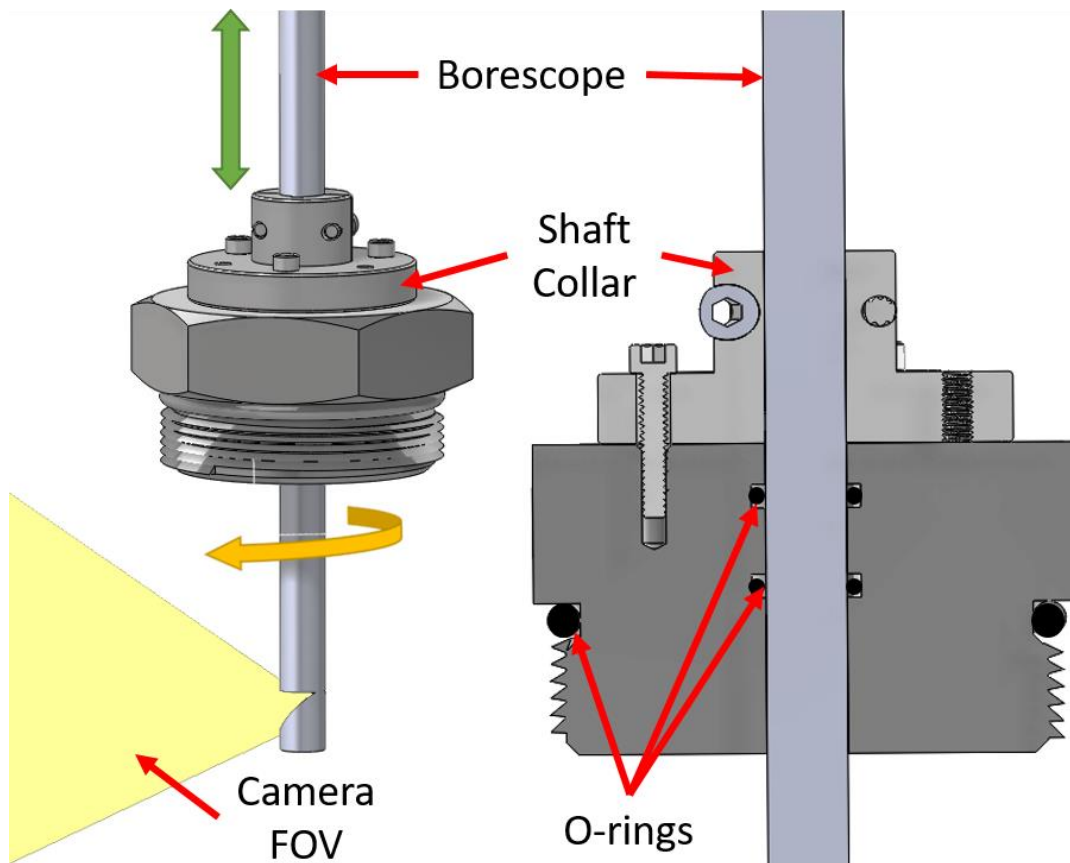


Figure 4.4. Details of the BRASTA borescope mount.

This is just one of many additional planes that can be investigated in BRASTA with the developed methodology. Nonetheless, it will help establish the application of endoscopic PIV to this facility, which is crucial to the development of optical diagnostic techniques for STARR.

#### 4.2 Evolution of Setup for 3D Velocity Measurements

To install the borescopes into the traverse ring on the rotating rig, a mounting system has been designed based on the apparatus that was successfully implemented with BRASTA for PSP measurements. It again features a shaft collar that provides identical freedom of movement, but an extended outer body was required to provide space for the flange of the collar as there is limited space between the upstream and downstream modules of the facility. These features, along with the locations of O-rings and the field of view afforded by the Gradient Lens Corp. borescope, are defined in Figure 4.5.

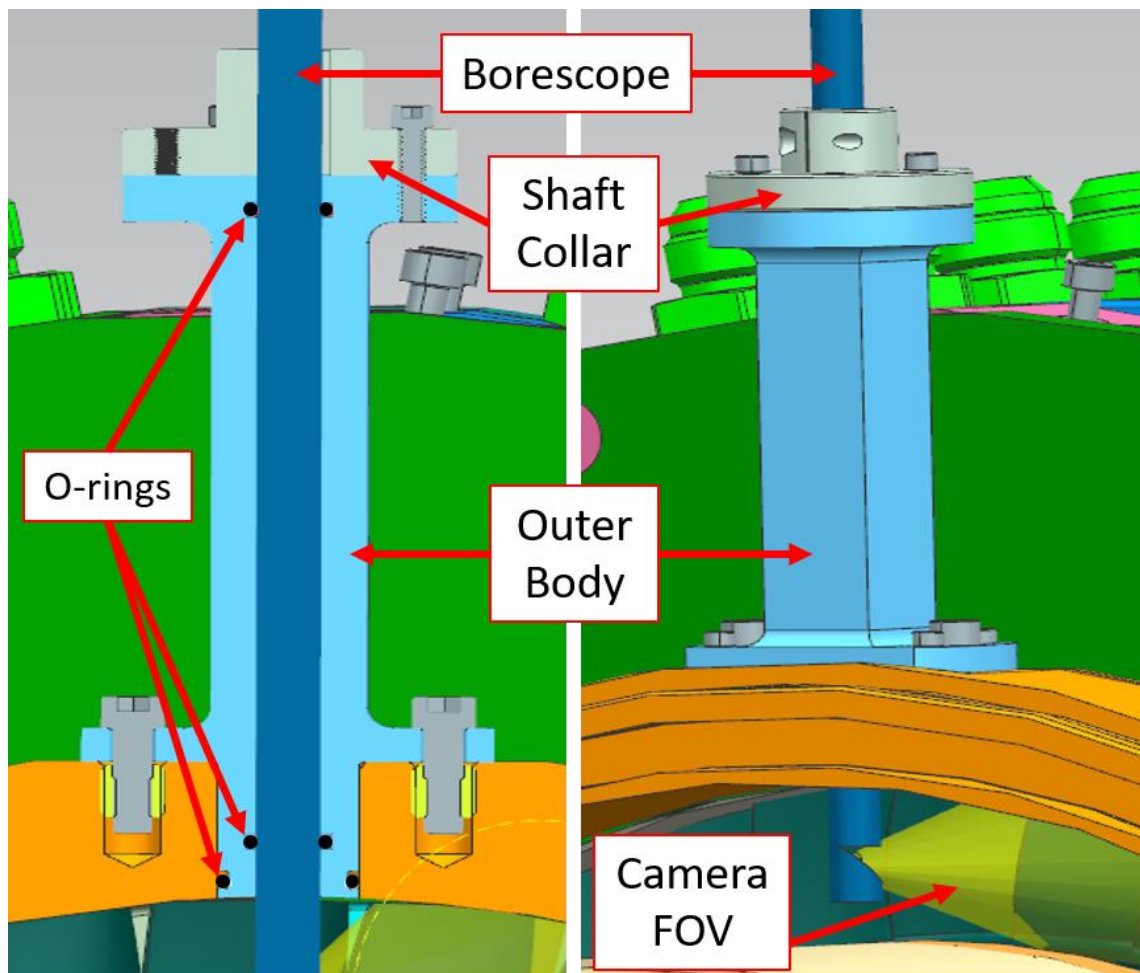


Figure 4.5. Details of the STARR borescope mount.

Finally, to deliver a laser sheet into the blade passage in the form of a radial plane, an insert was designed to provide direct over blade optical access. The insert features a large window at the bottom of the outer body that matches the curvature of the inner radius so that it can be flush mounted and not interfere with the sensitive blade passage flow. A window brace sits inside the outer body to fasten the optical window and seal it against the gasket, but it has a very low profile within the body to maximize the optical access for the incoming laser sheet. Both the outer body and window brace shown in Figure 4.6 have been machined out of stainless steel for the first and second rotor stages so that they are able to survive the harsh operating conditions of this rotating annular rig. Due to the proximity of the insert to the interrogation region, the sheet forming optics can be located outside of the laser delivery insert without concern of clipping the laser sheet.

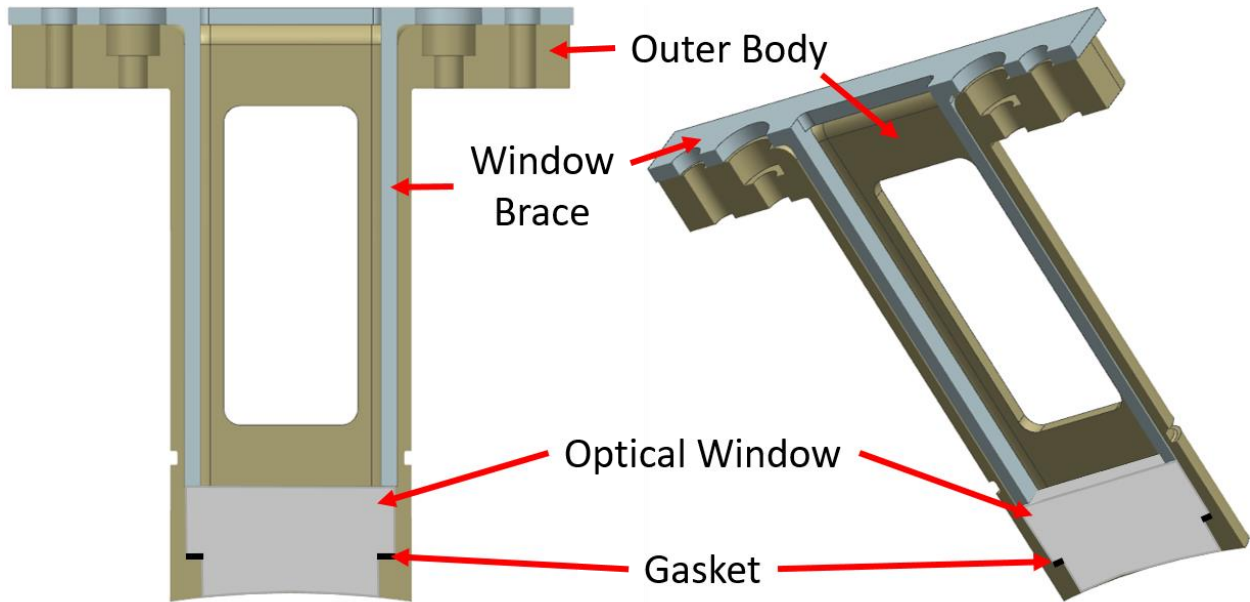


Figure 4.6. Details of the STARR laser delivery inserts.

With this SPIV configuration, a 3D velocity map can be resolved for the blade passage flow. This information will enable the identification of secondary flow structures and help characterize the tip leakage flows to assess the performance of the new tip design.

## 5. CONCLUSIONS

Particle image velocimetry was used in this work to measure the velocity components and flow angles in a central region of a vane passage within an annular cascade. The application of this optical measurement technique is especially challenging in annular cascades due to the limited optical access and the curvature of the surfaces. A methodology was developed to deliver a planar laser sheet into the vane passage and obtain particle scattering images for PIV within the PETAL BRASTA facility at cold and hot conditions.

The alignment and the laser delivery inside of the studied flow path were the two main practical challenges faced during the setup. Tailored optical hardware was designed to deliver the laser beam inside of the flow path, forming the laser sheet, and modifying the angle of the sheet to illuminate the desired measurement location. Careful alignment between the laser sheet illuminating the seed particles, the image plane of the camera, and the vane geometry was necessary for direct comparisons with CFD model predictions. Custom pre-processing algorithms were also developed to improve the vector yield and overcome challenges due to light scattering and image-to-image intensity variations.

The velocity measurements acquired in the vane passage, as well as the derived flow angles and the spatial distributions of both, are in good agreement with the CFD model predictions. Flow angles measured with 5-hole probes at the exit plane provided independent verification of the values reported by the CFD model predictions and the corresponding PIV measurements within the vane passage. Evaluation of the measurement technique also shows that the methodology produces high vector yields (close to 100%) for most of the measurement region at cold flow conditions, while at hot flow conditions the vector yield was in the range of 50-80%. As this work utilized a high-speed, burst-mode laser source and high-speed camera, this indicates that high-speed measurements are feasible, particularly at cold flow conditions, with room for additional improvements under hot flow conditions to reduce scattering and laser sheet intensity variations across the image plane. The uncertainty of the velocity measurements was estimated at ~1.5% using a correlation statistics-based method.

The establishment of this methodology also served as a building block for the development of endoscopic SPIV in STARR to aid in the non-intrusive characterization of tip flows in a rotating environment for assessing novel rotor tip designs. An experimental design for demonstrating the

feasibility of endoscopic PIV in PETAL facilities and capturing the unsteady formation of the HSV system on the leading edge of the new vane design is also described. With the custom optical components presented, the two proposed experimental setups are equipped to be implemented.

## REFERENCES

- [1] Raffel, M., Willert, C.E., Scarano, F., Kähler, C.J., Wereley, S.T. and Kompenhans, J., “Particle image velocimetry: a practical guide,” Springer, 2018. doi: 10.1007/978-3-540-72308-0.
- [2] Xue, Z., Charonko, J., Vlachos, P., 2014, “Particle image velocimetry correlation signal-to-noise ratio metrics and measurement uncertainty quantification,” *Journal of Measurement Science and Technology*, Vol. 25, No. 11. doi: 10.1088/0957-0233/25/11/115301.
- [3] Bloxham, M.J., 2010, “A Global Approach to Turbomachinery Flow Control: Loss Reduction Using Endwall Suction and Midspan Vortex Generator Jet Blowing,” Ph.D. dissertation, The Ohio State University, Columbus, OH.
- [4] Marks, C., Sondergaard, R., Wolff, M. and Estevadeordal, J., 2009, “PIV Investigation of a Highly-Loaded LPT Blade Using a Curved Laser Sheet,” 47th AIAA Aerospace Sciences Meeting. doi: 10.2514/6.2009-301.
- [5] Gross, A., Marks, C.R., Sondergaard, R., Bear, P.S. and Mitch Wolff, J., 2017, “Experimental and numerical characterization of flow through highly loaded low-pressure turbine cascade,” *Journal of Propulsion and Power*, Vol. 34, No. 1, pp. 27-39. doi: 10.2514/1.B36526.
- [6] Bear, P., Wolff, M., Gross, A., Marks, C.R. and Sondergaard, R., 2018, “Experimental investigation of total pressure loss development in a highly loaded low-pressure turbine cascade,” *Journal of Turbomachinery*, Vol. 140, No. 3. doi: 10.1115/1.4038413.
- [7] Peter, J., Pardowitz, B., Eck, M., Enghardt, L., Peitsch, D. and Thamsen, P., 2017, “Advanced Stereo High-Speed PIV in an Annular Cascade without Clearance: Evidences of Rotating Instability,” 12<sup>th</sup> European Conference on Turbomachinery Fluid dynamics & Thermodynamics. doi: 10.29008/ETC2017-205.
- [8] Anderson, C., Lynch, S., 2015, “Time Resolved Stereo-PIV Measurements of the Horseshoe Vortex System in a Low Aspect Ratio Pin-Fin Array,” 51<sup>st</sup> AIAA/SAE/ASEE Joint Propulsion Conference, Propulsion and Energy Forum. doi: 10.1007/s00348-015-2091-7.

- [9] Woisetschläger, J., Göttlich, E., 2007, "Recent Applications of Particle Image Velocimetry to Flow Research in Thermal Turbomachinery." In: Particle image velocimetry. Topics in Applied Physics, Vol. 112. doi: 10.1007/978-3-540-73528-1\_16.
- [10] Gostelow, J.P., Mahallati, A., Carscallen, W.E., Rona, A., 2012, "Encounters with Vortices in a Turbine Nozzle Passage," International Journal of Rotating Machinery, Vol. 2012. doi: 10.1155/2012/928623.
- [11] Cuadrado, D.G., Aye-Addo, P. A. N., Andreoli, V., Bhatnagar, L., Lozano, F., Paniagua, G., Inman, D., Fisher, J., Saavedra, J., Meyer, T., Bloxham, M., Clemens, E., Stults, B., White, T., Wallace, A., Johnson, D., 2019, "Purdue Small Turbine Aerothermal Rotating Rig (STARR)," AIAA Propulsion and Energy 2019 Forum. doi: 10.2514/6.2019-4004.
- [12] Kegalj, M., Schiffer, H.P., 2008, "Endoscopic PIV Measurements in a Low-Pressure Turbine Rig," Journal of Experiments in Fluids, Vol. 47. doi: 10.1007/s00348-009-0712-8.
- [13] Reeves, M., Lawson, N.J., 2004, "Evaluation and correction of perspective errors in endoscopic PIV," Journal of Experiments in Fluids, Vol. 36. doi: 10.1007/s00348-003-0746-2.
- [14] Paniagua, G., Cuadrado, D.G., Saavedra, J., Andreoli, V., Meyer, T., Solano, J. P., Herrero, R., Meyer, S., and Lawrence, D., 2018 "Design of the Purdue Experimental Turbine Aerothermal Laboratory for Optical and Surface Aerothermal Measurements," Journal of Engineering for Gas Turbines and Power, Vol. 141, No.1. doi:10.1115/1.4040683.
- [15] M. N. Slipchenko, J. D. Miller, S. Roy, J. R. Gord, S. A. Danczyk, and T. R. Meyer, "Quasi-continuous burst-mode laser for high-speed planar imaging," *Opt. Lett.*, vol. 37, no. 8, p. 1346, 2012.
- [16] Smyser, M.E., Rahman, K.A., Slipchenko, M.N., Roy, S., and Meyer, T.R., 2018, "Compact burst-mode Nd:YAG laser for kHz–MHz bandwidth velocity and species measurements," *Opt. Lett.* Vol. 43, No. 4, pp. 735-738. doi: 10.1364/OL.43.000735.
- [17] Lauriola D.K., Gomez, M., Meyer, T.R., Son, S.F., Slipchenko, M.N., and Roy, S., 2019. "High Speed Particle Image Velocimetry and Particle Tracking Methods in Reactive and Non-Reactive Flows," AIAA SciTech Forum. doi: 10.2514/6.2019-160.

- [18] Sciacchitano A., 2019, “Uncertainty Quantification in Particle Image Velocimetry,” *Journal of Measurement Science and Technology*, Vol. 30, No. 9. doi: 10.1088/1361-6501/ab1db8.
- [19] LaVision, 2018, “PIV Uncertainty Quantification,” DaVis 8.4.0., June 2018, LaVision GmbH, Anna-VandenHoeck-Ring 19, D-37081.